

A numerical study on precipitation over the western coastal area of Sumatra Island

Ryosuke Okugawa¹, Kazuaki Yasunaga¹, and Atsushi Hamada¹

¹University of Toyama

November 23, 2022

Abstract

It has been documented that significant amounts of tropical precipitation are concentrated in coastal areas, which is especially prominent over the western coast of Sumatra Island. We conducted 14-day-long numerical simulations, focusing on precipitation patterns around Sumatra Island. In the control experiment, the rainfall concentration was obscure, and dry biases were found. Based on the budget equation of the column-integrated frozen moist static energy (which is nearly equivalent to the column-integrated moisture under the weak temperature gradient assumption), we formulated 9 sensitivity experiments. When the terminal velocity and effective radius of ice clouds were reduced in addition to incorporating the warmer sea surface temperature (SST) around the coast, the model showed better rainfall peak fidelity. On the other hand, similar diurnal cycles of precipitation were simulated in the sensitivity tests without any conspicuous peaks in the coastal region, which indicated that the precipitation concentration fidelity was irrelevant to that of the diurnal cycle. An analysis in the time-mean fields demonstrated that inhibition of radiative cooling (associated with the upper-level ice clouds) and warmer SSTs induced anomalous updrafts, and thus, more moisture and precipitation were brought to the coast by enhancement of the vertical moisture advection. Comparing the simulation results with in situ observations, we speculated that together with the climatologically warmer SSTs, the SST diurnal cycle and lateral transport of ice clouds from inland convection, which was strictly regulated by solar insolation, significantly contributed to the precipitation concentration around the coastal region.

A numerical study on precipitation over the western coastal area of Sumatra Island

Ryosuke Okugawa¹, Kazuaki Yasunaga¹, and Atsushi Hamada¹

¹ Department of Earth Science, Graduate School of Science and Engineering, University of Toyama, Toyama, Japan.

Corresponding author: Kazuaki Yasunaga (yasunaga@sus.u-toyama.ac.jp)

†Department of Earth Science, Graduate School of Science and Engineering, University of Toyama, Gofuku 3190, Toyama-city, Toyama 930-8555, Japan

Key Points:

- Numerical experiments are conducted to simulate the precipitation concentration in the western coastal area of Sumatra Island.
- More abundant upper-level ice clouds and warmer SSTs are important for better rainfall concentration fidelity over the coastal area.
- The SST diurnal cycle and lateral transport of ice clouds from inland convection contribute greatly to the precipitation concentration.

Abstract

It has been documented that significant amounts of tropical precipitation are concentrated in coastal areas, which is especially prominent over the western coast of Sumatra Island. We conducted 14-day-long numerical simulations, focusing on precipitation patterns around Sumatra Island. In the control experiment, the rainfall concentration was obscure, and dry biases were found. Based on the budget equation of the column-integrated frozen moist static energy (which is nearly equivalent to the column-integrated moisture under the weak temperature gradient assumption), we formulated 9 sensitivity experiments. When the terminal velocity and effective radius of ice clouds were reduced in addition to incorporating the warmer sea surface temperature (SST) around the coast, the model showed better rainfall peak fidelity. On the other hand, similar diurnal cycles of precipitation were simulated in the sensitivity tests without any conspicuous peaks in the coastal region, which indicated that the precipitation concentration fidelity was irrelevant to that of the diurnal cycle. An analysis in the time-mean fields demonstrated that inhibition of radiative cooling (associated with the upper-level ice clouds) and warmer SSTs induced anomalous updrafts, and thus, more moisture and precipitation were brought to the coast by enhancement of the vertical moisture advection. Comparing the simulation results with in situ observations, we speculated that together with the climatologically warmer SSTs, the SST diurnal cycle and lateral transport of ice clouds from inland convection, which was strictly regulated by solar insolation, significantly contributed to the precipitation concentration around the coastal region.

Plain Language Summary

It has been documented that significant amounts of tropical precipitation are concentrated in coastal areas, which is especially prominent over the western coast of Sumatra Island. The present study conducted 14-day-long numerical simulations, focusing on precipitation patterns around Sumatra Island. In the control experiment, the rainfall concentration was obscure, and dry biases were found. However, the model showed improvements in the rainfall peak fidelity, when the terminal velocity and effective radius of ice clouds were reduced in the cloud microphysics parameterization in addition to incorporating the warmer sea surface temperature (SST) around the coast. An analysis in the time-mean fields (such as water vapor, ice clouds, radiative heating etc.) demonstrated that inhibition of radiative cooling (associated with the upper-level ice clouds) and warmer SSTs induced anomalous updrafts, and thus, more moisture and precipitation were brought to the coast by enhancement of the vertical moisture transport. Comparing the simulation results with in situ observations, it was speculated that together with the climatologically warmer SSTs, the SST diurnal cycle and lateral transport of ice clouds from inland convection, which was strictly regulated by solar insolation, significantly contributed to the precipitation concentration around the coastal region.

1. Introduction

The maritime continent (MC) consists of a complex organization of islands with a variety of sizes positioned amid warm surface waters of the tropical western Pacific Ocean and eastern Indian Ocean. Since the early years, global measurements by satellites have repeatedly demonstrated that the moist and warm environments of the MC host one of the most active convection centers worldwide (e.g., Heddinghaus & Krueger, 1981; Liebmann & Hartmann, 1982; Salby et al., 1991). The latent heat associated with vigorous convection are considered to be a primary source for driving the atmospheric general circulation and circulation within the tropics (e.g., Ramage 1968; Chang & Lau, 1982). In addition, Rossby wave trains associated with MC convection distort atmospheric flow patterns at higher latitudes, and the weather and climate are influenced on the global scale (e.g., Stan et al., 2017; Yang et al., 2019). Accordingly, convective storms and associated precipitation over the MC have significantly attracted both tropical and middle-latitude meteorologists, and numerous field experiments have been conducted to elucidate convective activities there (e.g; Houze et al., 1981; Keenan et al., 1989; Yihui et al., 2004; Keenan et al., 2000; Fukao, 2006; Yamanaka, 2016; Yokoi et al., 2017; Mori et al., 2018; Yokoi, 2020).

The intricate topography forms lengthened coastlines over the MC. Intensive radiative forcing by the sun in the lower latitudes and land-sea contrasts of the heat capacity along the elongated coastlines predominantly drive local- or regional-scale circulations with a diurnal cycle. The development of deep convection is strictly regulated by the pronounced daily pulse of the land-sea (breeze) circulation. Therefore, great attention from prior observational works has been oriented to diurnal variations. Currently, a typical picture of the diurnal cycle is well illustrated; the sea breeze initiates convection in the afternoon over the elevated orography together with mountain-valley breezes, and precipitation peaks there in the late afternoon and early evening around the foothills, while precipitation reaches a maximum in the early morning over the open ocean. In addition, over the coastal area, the precipitation peak propagates from the landside to the seaside coastal regions, connecting the two maxima of the diurnal cycle over the land and open ocean. Although intensively collected in situ data have been mostly confined to a limited region and there are different observed behaviors of the diurnal cycle in different locations, these diurnal cycle regimes of convection (land, ocean, and coastal regimes) are robust over the entire tropics, with the aid of horizontally quasi-homogeneous satellite observations (e.g., Hendon and Woodberry 1993; Dai 2001; Yang & Slingo, 2001; Nesbitt & Zipser, 2003; Mori et al., 2004; Yang and Smith 2006; Kikuchi & Wang, 2008).

Despite our better understanding of the rainfall diurnal cycle, several fundamental issues remain unresolved in association with convective storms over the MC. Among them, rainfall concentrations near tropical coastlines are the most crucial in terms of the hydrological cycle and the pivotal role of latent heat. The heaviest precipitation is brought to the eastern coasts over the Bay of Bengal and Arabian Sea (e.g., Grossman & Durran, 1984; Ogura & Yoshizaki, 1988; Zuidema, 2003; Xie et al., 2006; Shige et al., 2017). Similar features are also found in northwestern South America (e.g., Mapes et al., 2003). More comprehensively, Bergemann et al. (2015) quantitatively showed that in the regions where land-sea interactions play a crucial role in the formation of precipitation, 40%-60% of the total rainfall can be related to coastline effects. Later, Ogino et al. (2016) indicated that the tropical rainfall distribution is approximately expressed by a function of the coastal distance with dominance on the seaside. However, the reality is more complex, even if the MC and its adjacent regions are the subject of focus. For example, the seaside peak is especially pronounced along the western coast of Sumatra Island and the Indochina

Peninsula (around Myanmar), while the rainfall concentrations are obscure or barely visible along the northern, southern, and eastern coasts over the MC (e.g., Fig. 1a). Furthermore, rainfall peaks are located around the elevated orography on the Borneo and New Guinea Islands, which are surrounded by warmer sea surface temperatures (SSTs) (e.g., Fig. 1b). Therefore, SST distributions alone cannot account for the precipitation patterns, although it is likely that climatologically warmer SSTs in the MC contribute to the formation of coastline rainfall peaks to some extent.

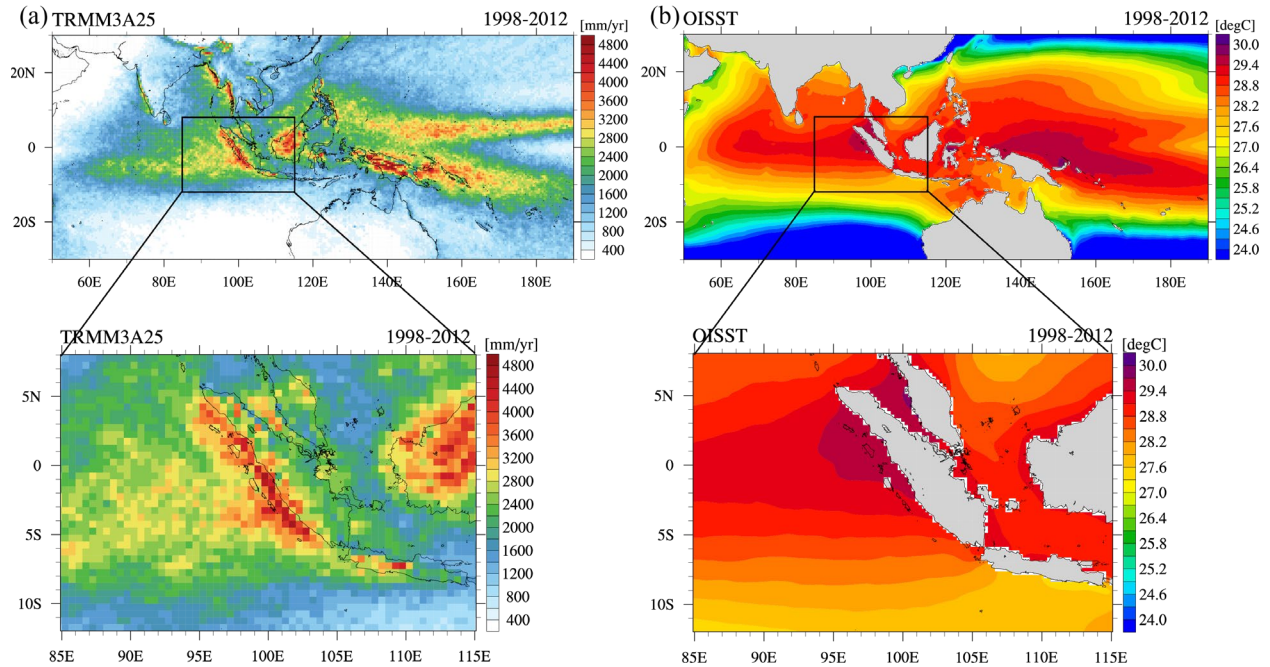


Figure 1: Geographical distributions of climatological (15-year mean) precipitation (a) and SST (b). Lower panels represent close-up views of the rectangular area in (a) and (b). Precipitation and SST distributions are based on TRMM 3A25 (e.g., Kummerow et al., 2000) and OI-SST (e.g., Reynolds et al., 2007) datasets, respectively.

Coastal rainfall is associated with the seaward migration of land-originated convective systems (e.g., Sakurai et al., 2005, 2009; Mori et al., 2011; Yanase et al., 2017). In terms of the “passage” of the convective system, several mechanisms have been proposed, such as gravity waves (e.g., Mapes et al., 2003; Hassim et al., 2016; Yokoi et al., 2017), the interaction of local winds and environmental monsoonal winds (e.g., Houze et al. 1981; Grossman & Durran, 1984; Ogura & Yoshizaki, 1988), the interaction of cold outflow from convective downdraft and environmental winds (e.g., Mori et al., 2004; Wu et al., 2008, 2009), and advection by the environmental winds associated with larger-scale disturbances (e.g., Ichikawa & Yasunari, 2006; Shige et al. 2017; Sakaeda et al., 2020). However, the mechanisms for the “concentration” along the coastlines are unexplained. Motivated by such an incomplete understanding, we conducted numerical simulations in the present investigation using a cloud-system resolving model to seek clues about the mechanism of the coastline rainfall concentration. For our purpose, the numerical

experiments target Sumatra Island and the adjacent ocean, where the seaside peak of precipitation is the most prominent with warmer SSTs (Figs. 1a and 1b).

It is well-known that general circulation models (GCMs) unsatisfactorily reproduce the climatological precipitation patterns over the MC (e.g., Neale & Slingo, 2003; Toh et al., 2018). With regard to the rainfall concentrations, the horizontal resolutions of GCMs are generally insufficient. However, recent progress in computer resources has allowed us to conduct global or regional (climate) simulations with a horizontal grid spacing of less than 20 kilometers. Although such high-resolution GCMs successfully reproduce basic features of the rainfall diurnal variations, there are still substantial biases in precipitation patterns over the MC (e.g., Arakawa & Kitoh, 2005; Mizuta et al., 2006; Hara et al., 2009; Bhatt et al., 2016; Im & Eltahir, 2018; Kim et al., 2019). Recent model intercomparisons revealed that performances of the land-ocean contrast of daily mean precipitation and amplitude of the diurnal cycle are uncorrelated (Baranowski et al., 2019). Therefore, it is desirable to mitigate model biases, exclusively focusing on the precipitation distributions over the MC, although both the better reproduction of the precipitation patterns and variations significantly rely on the cumulus parameterization (e.g., Ulate et al., 2014).

Cloud/cloud-system resolving models (CRMs) with a grid-spacing of several kilometers have also been extensively employed to investigate convective storms over the MC in collaboration with or independently of field experiments (e.g., Wu et al., 2008, 2009; Sato et al., 2009; Fujita et al., 2011; Hassim et al., 2016; Vincent & Lane, 2016). The fidelity of the precipitation diurnal cycle simulated by CRMs is generally better than that of GCMs. However, not all CRMs reproduce the seaside rainfall peaks along the coastline, although cumulus parameterization is not applied in the simulations. For example, negative rainfall biases prevail, and no peaks are found along the western coast of Sumatra Island in the simulations by Vincent & Lane, (2017) and Argüeso et al. (2019), while the UK Met Office atmospheric model with a horizontal resolution of 4 km reproduces realistic rainfall distributions (Love et al., 2011). These results indicate that fidelity of the climatological precipitation patterns (at least the coastline rainfall concentration) would be irrelevant to the better representation of the diurnal cycle by CRMs as well as GCMs.

Therefore, our approach here is that the fidelity of the mean precipitation patterns around Sumatra Island is primarily evaluated and little emphasis is added to the performances of the diurnal cycle, although the relationships between the mean precipitation patterns and diurnal variations in convection are discussed. More specifically, sensitivity experiments regarding cloud microphysics and surface heat fluxes are systematically programmed, focusing on the moist static energy budgets (or moisture budgets under the weak temperature gradient assumption; see section 2 for more detail) over the coastal region and open ocean, since the well-known relationships between precipitation and column-integrated moisture (e.g., Bretherton et al., 2004) are valid in coastal areas as well as over the open ocean (e.g., Bergemann & Jakob, 2016). Furthermore, processes of rainfall concentration along the coastline are highlighted based on the results of sensitivity tests, which show better performances in moist static energy (or moisture) budgets.

The remainder of the paper is organized as follows: section 2 briefly describes the model setting and general designs for the numerical experiments, the results of the control experiment are overviewed in section 3, the designs for the sensitivity tests are elaborated in section 4, the results of the sensitivity tests are compared in section 5, the fidelity of the diurnal cycles are examined in section 6, the possible mechanism for the rainfall concentration along the coastline is discussed in section 7, and section 8 summarizes the results.

2. Model description and experimental design

We performed numerical simulations by using ver. 5.2.5 of the Scalable Computing for Advanced Library Environment-Regional Model (SCALE-RM). The model was developed as a meteorological large-eddy simulation model in the RIKEN Center of Computational Science (R-CCS), Japan. The basic equations and a description of the numerical model can be found in Nishizawa et al. (2015) and Sato et al. (2015). SCALE-RM has been tested for several actual events and ideal cases (e.g., Sueki et al., 2019; Yoshida et al., 2019; Tanji & Inatsu, 2019).

The model domain covers the eastern Indian Ocean and Sumatra Islands (Fig. 1b). The horizontal grid size is 3.5 km. The model has 80 layers in the vertical direction (model top at 24 km), with a fine grid spacing (40 m) in the lowest level and a relatively coarse grid spacing (360 m) in the upper levels. Initial and (lateral and surface) boundary conditions are linearly interpolated from the National Centers for Environmental Prediction Final Operational Global Analysis (NCEP-FNL) data, which have a $1^\circ \times 1^\circ$ horizontal grid size and are provided every 6 hours. Although the grid spacing of 3.5 km is not able to adequately resolve a convection core, no cumulus parameterization is employed. Instead, moist processes are represented using a six-category (water cloud, rain, ice cloud, snow, and graupel) single-moment bulk scheme (Tomita, 2008). PBL turbulence and radiation schemes are based on Nakanishi & Niino, (2009) and Sekiguchi & Nakajima, (2008), respectively.

Numerical integrations start on 22 November 2015 and end on 7 December 2015. The initial 24-hour simulation is assumed to be a spin-up period, and 14-day-long results are compared. We chose this period because the mean precipitation shows a prominent seaside peak along the western coast of Sumatra Island (Fig. 2a), which is similar to the climatological rainfall distributions (Fig. 1a). The other reason for setting these simulation dates is that the international field campaign Pre-YMC was conducted in November–December of 2015 in the western coastal area of Sumatra Island by the Japan Agency for Marine–Earth Science and Technology (JAMSTEC), the Indonesian Agency for the Assessment and Application of Technology (BPPT), and the Indonesian Agency for Meteorology, Climatology and Geophysics (BMKG). Intensive observations were performed by the R/V Mirai of JAMSTEC; the observations were collected at approximately 4.078 S, 101.908 E, and at the BMKG observatory in Bengkulu city at 3.868 S, 102.348 E (more detailed descriptions of the Pre-YMC campaign can be found in Yokoi et al. (2017)). The data obtained in the campaign (such as radiosonde soundings and surface meteorological observations) are incorporated into the operationally analyzed fields through the Global Telecommunication System (GTS) of the World Meteorological Organization (WMO). Therefore, we can expect better quality of the initial and boundary data (NCEP-FNL) in this period, and we can easily evaluate the model performances through comparisons with the Pre-YMC observations.

3. Overview of the control experiment

To give an overview of the cloud and precipitation fields during the integration periods, Figs. 2a, 2b, and 2c present the time-mean precipitation derived from the Global Satellite Mapping of Precipitation (GSMaP; Okamoto et al., 2005), outgoing longwave radiation retrieved from NOAA's polar-orbiting satellites (OLR; Liebmann & Smith, 1996), and column-integrated water vapor (CWV) of NCEP-FNL. In the simulation period, clouds were organized over the eastern Indian Ocean in association with the active phase of the Madden–Julian oscillation (MJO; Madden & Julian, 1971, 1972), and in the western coastal area of Sumatra Island, the diurnal variations in

precipitation were prominent (e.g., Yokoi et al., 2017), as is typically seen when the MJO convective envelope is located over the eastern Indian Ocean (e.g., Fujita et al., 2011; Kamimera et al., 2012). Reflecting on the pronounced diurnal cycle, large amounts of precipitation were brought to the western coast of Sumatra Island with dominance on the sea side, which is close to the climatological distributions of precipitation (Fig. 1a). Corresponding to the precipitation distributions, a minimum OLR is located over the coastlines, and larger CWVs are found over the coastal oceanic region.

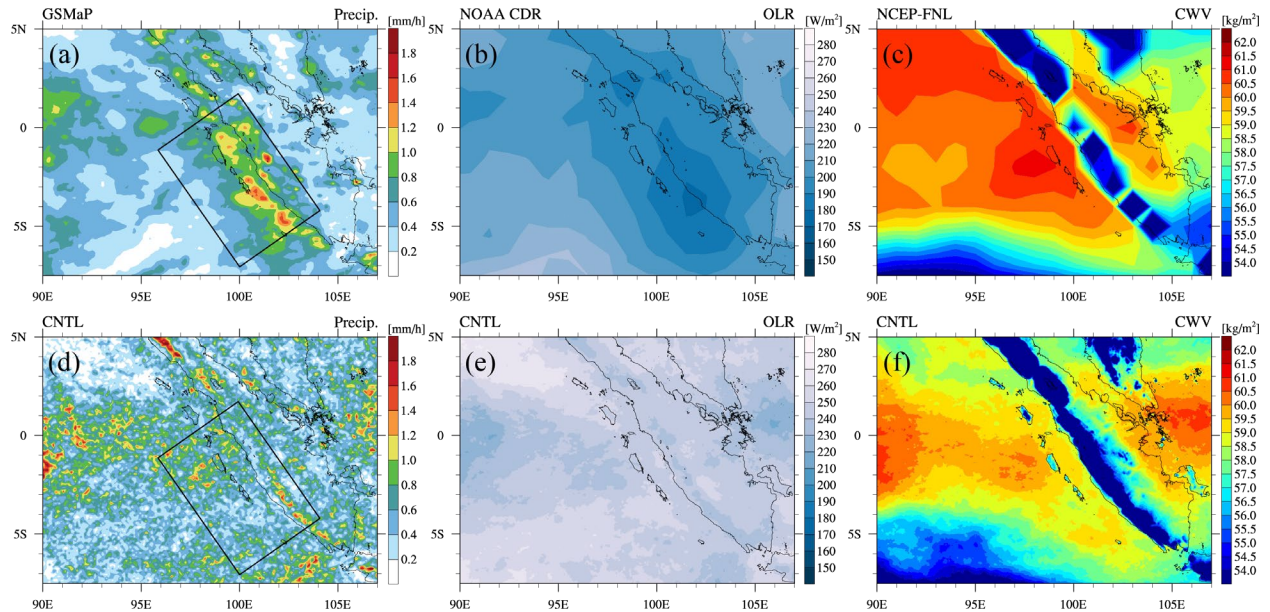


Figure 2: Geographical distributions of satellite-retrieved precipitation (a), OLR (b), and analyzed CWV (c) averaged over the simulation period (23 November - 7 December 2015). Lower panels represent the corresponding fields (d: precipitation, e: OLR, and f: CWV) that were simulated in the control experiment.

The control experiment calculates peaks in the time-mean precipitation at the elevated orography instead of the coastal ocean (Fig. 2d). In addition, simulated rainfall is more scattered over the domain than the retrieved precipitation. While CWV shows more homogeneous features (Figs. 2e and 2f), OLR and CWV are overestimated and underestimated around the western coast of Sumatra Island, respectively, which corresponds with the lack of rainfall concentration. These results indicate that our numerical model failed to reproduce the coastal rainfall peak using default physical parameterization settings. However, it should be emphasized that poor fidelity is not a unique problem of SCALE-RM; this issue is shared among most of the available numerical models. For example, the Weather Research and Forecasting (WRF) model, which is the most popular community tool for mesoscale meteorology, also represents similar deficiencies in prior works, as described in the introduction. In addition, general features of the time variations in the radiosonde-derived winds are well captured in the control experiment (Fig. 3). Therefore, a series of sensitivity tests aiming to improve the fidelity of the precipitation peak would serve as methodological inspiration for additional numerical studies.

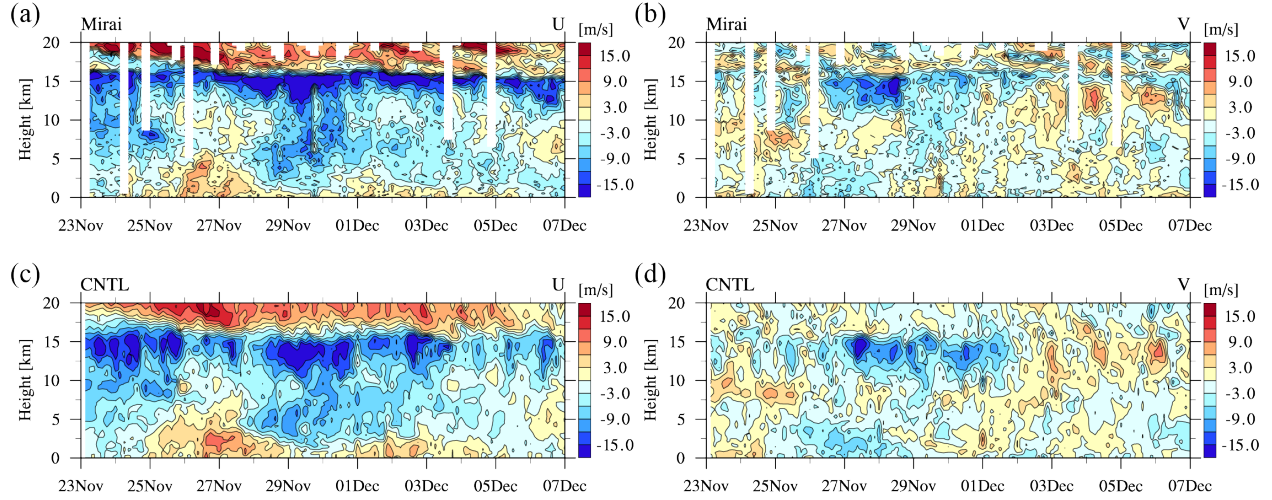


Figure 3: Time-height cross section of the zonal (a) and meridional (b) winds derived from radiosonde soundings during the simulation period (23 November - 7 December 2015) at the stationary observation point of the R/V Mirai. Lower panels represent the corresponding fields (c: zonal wind, and d: meridional wind) simulated in the control experiment.

4. Formulation of sensitivity experiments

It is well known that precipitation is monotonically dependent on CWV over the tropical open ocean (e.g., Bretherton et al. 2004; Neelin et al., 2009; Mapes et al., 2018; Rushley et al., 2018). These monotonic relationships between moisture and precipitation are weak or obscure over land (e.g., Schiro et al., 2016; Ahmed & Schumacher, 2017). However, similar behavior is still confirmed in coastal areas (e.g., Bergemann & Jakob, 2016), at least around the western coast of Sumatra Island (Ahmed & Schumacher, 2017). In fact, our control experiment represents both smaller amounts of CWV and little precipitation around the coastal ocean. Since the water vapor field has a spatially homogeneous character in comparison with (more localized) precipitation, we should focus on the CWV budget equation for the formulation of sensitivity tests instead of precipitation itself. However, the CWV budget equation includes precipitation. Therefore, the budget equation of the frozen moist static energy (FMSE) is actually used to improve the precipitation patterns. FMSE (m) is expressed as follows.

$$m = s + L_v q_v - L_f q_i$$

where s is dry static energy, L_v is the latent heat of vaporization, L_f is the latent heat of fusion, q_v is the water vapor mixing ratio, and q_i is a mixing ratio of all ice phase condensates (ice cloud, snow, and graupel). The column-integrated FMSE (CFMSE) budget equation is given as follows:

$$\left\langle \frac{\partial m}{\partial t} \right\rangle = -\langle \mathbf{v} \cdot \nabla m \rangle + \langle Q_R \rangle + (H + L_v E), \quad (1)$$

where \mathbf{v} is the three-dimensional wind vector, Q_R is net radiative heating rate, H is sensible heat flux from the surface, E is surface evaporation, and the angle brackets indicate mass-weighted column integration. Under the weak temperature gradient (WTG) approximation (Sobel et al., 2001), the evolution of CFMSE determined by Eq. (1) is nearly equivalent to CWV. Namely,

$$L_v \left\langle \frac{\partial CWV}{\partial t} \right\rangle \approx -\langle \mathbf{v} \cdot \nabla m \rangle + \langle Q_R \rangle + (H + L_v E). \quad (2)$$

We formulate sensitivity experiments regarding cloud microphysics and surface heat fluxes to increase CWV through radiative heating and surface heat fluxes in Eq. (2). Here, 5 sensitivity tests are conducted: the terminal velocity and effective radius of ice clouds are reduced (ICE), intercept parameters of snow and graupel are modified in reference to Wainwright et al. (2014) (WW14M), cloud droplets are downsized (CLOUD), an intercept parameter of rain is 10 times larger than the original value (NOR10), and SST products are replaced (SST). In the remainder of this section, those tests are elaborated together with the associated backgrounds. Cloud microphysics is a highly nonlinear process. Atmospheric motions responded to the released latent heat advect water vapor. Similarly, the momentum transport by convective downdrafts affects moisture transfer from the surface. As a result, the probability of subsequent convection development changes. Such feedback makes the simulation results difficult to predict. Therefore, it should be noted that some experiments would certainly present negative results against our expectations described below.

In the ICE experiment, parameterization of the terminal velocity of ice clouds (v_{Ti}) is refined. In the default setting, v_{Ti} is determined only from mixing ratios of ice clouds, following Heymsfield & Donner (1990). The parameterization of v_{Ti} is updated by in situ observations in low-latitude ice cloud layers, which was proposed by Heymsfield et al. (2007). In the newly incorporated scheme, v_{Ti} is dependent on the ambient temperature as well as the mixing ratios. Consequently, v_{Ti} becomes significantly smaller around the tropopause (close to $0 \text{ m} \cdot \text{s}^{-1}$), where the temperature reaches a minimum. In addition, the effective radius of ice clouds is modified to be dependent on temperature, while it is assumed to be a constant ($40 \text{ } \mu\text{m}$) in the original radiation scheme. The empirical relationships between the effective radius and temperature are found by Thornberry et al. (2017), based on cirrus cloud observations in the tropical tropopause layer over the western Pacific. We can expect that both modifications in the ICE experiment result in enhancement of the radiative heating through lengthened lifetime and profound optical thickness of ice clouds if other terms (advection, and surface heat fluxes) remain the same.

In the WW14M experiment, intercept parameters of snow and graupel are replaced from $3.0 \times 10^6 \text{ m}^{-4}$ and $4.0 \times 10^6 \text{ m}^{-4}$ to $3.95 \times 10^8 \text{ m}^{-4}$ and $5.26 \times 10^7 \text{ m}^{-4}$, respectively. These values are derived from supercell storm simulations using the double-moment cloud microphysics scheme, in which coverage of stratiform precipitation is profoundly extended (Wainwright et al., 2014). In addition, the upper limits of the collection efficiency of snow for cloud ice (E_{si}) and graupel for snow (E_{gs}) are lowered from 1.0 to 0.1, referring to successful simulations of tropical anvil clouds by previous works (e.g., Krueger et al., 1995; Lang et al., 2007). Diabatic heating profiles associated with convective and stratiform precipitation are different; convective heating is positive throughout the profile, while the stratiform heating profile is characterized by upper-level heating and lower-level cooling (e.g., Houze, 2004). This dipole structure of stratiform heating imports dry-air in the mid-troposphere and effectively reduces CWV (e.g., Holloway & Neelin, 2009; Yasunaga & Mapes, 2012). On the other hand, it is possible that extended areas of stratiform precipitation compete with the damping effect through the suppression of longwave cooling. Such cloud-radiation feedback is attributed to the development of the MJO (e.g., Lin & Mapes, 2004; Andersen & Kuang, 2011; Sobel et al., 2014; Janiga & Zhang, 2016; Kim et al.,

2015; Wolding & Maloney, 2015; Adames & Kim, 2016; Yasunaga et al., 2018; Inoue et al., 2020 and many others). Mesoscale ascent in the stratiform region is primarily maintained by vapor deposition onto the growing ice particles (e.g., Houze, 1997). Larger intercept parameters mean more number concentrations of snow and graupel for a given mixing ratio, which provides more favorable conditions for vapor deposition growth of snow and graupel. Therefore, it is possible that the WW14M experiment leads to more extended areas of stratiform precipitation and increases CWV by inhibiting radiative cooling if cloud-radiation feedback exceeds the damping effect.

In the CLOUD experiment, the effective radius of cloud droplets is downsized by half (from 8 μm to 4 μm) for the radiation scheme. This downsizing is intended to increase the optical thickness of water clouds, as in the ICE experiment. However, the value of 4 μm is subjectively determined without any backing of the previous investigations. Nevertheless, we conducted this experiment for completeness to clarify the relative importance of condensate species in cloud-radiative feedback (rain drops have negligible effects on radiation). In fact, some idealized numerical simulations suggest that shortwave heating from low clouds is essentially important to the CWV increase in relatively humid regions (e.g., Wing & Emanuel, 2014), while strong longwave cooling makes dry regions drier (e.g., Muller & Held, 2012). Therefore, if the former mechanism works more effectively, larger amounts of CWV are expected in the CLOUD experiment.

In the NOR10 experiment, an intercept parameter of rain is replaced from $8.0 \times 10^6 \text{ m}^{-4}$ to $8.0 \times 10^7 \text{ m}^{-4}$. Numerous observational studies indicate that surface heat fluxes are enhanced due to the intensive wind speed in association with convective systems (e.g., Johnson & Nicholls, 1983; Young et al., 1995; Saxen & Rutledge, 1998; Esbensen & McPhaden, 1996; Chuda et al., 2008; Zuidema et al., 2011; Yokoi et al., 2014). The strong wind speed is accompanied by temperature decreases (cold pool), and evaporation of rain water is primarily responsible for intensification of the wind speed (and enhancement of the heat fluxes). Morrison et al., (2009) compared squall line simulations with single-moment and double-moment versions of the cloud-microphysical scheme and found that the reduced and increased rates of rain evaporation associated with smaller and larger intercept parameters result in weak and strong cold pools, respectively. Therefore, the larger intercept parameter of $8.0 \times 10^7 \text{ m}^{-4}$, which is based on their double-moment-scheme simulation, would lead to enhancement of the surface heat fluxes and thus the increase in CWV.

In the control experiment, SST, as the lower boundary condition, is initialized and updated every 6 hours with NCEP-FNL. It is generally difficult for the coarse horizontal grid size of NCEP-FNL ($1^\circ \times 1^\circ$) to adequately resolve the complicated topography over the MC. In addition, we notice that the analysis SST products are colder than the Pre-YMC offshore observations by R/V Mirai in the first half of the period (Fig. 4d). Dipankar et al. (2019) found that coastal SSTs have nonnegligible impacts on the numerical model fidelity in representing the precipitation diurnal cycle. Therefore, in the SST experiment, NCEP-FNL SST datasets are replaced with high-resolution SST analysis (OI-SST) provided by NOAA (Reynolds et al., 2007). The NOAA products show warmer SST distributions around the western coast of Sumatra Island (Figs. 4a, 4b, and 4c), and the time series are closer to the observations (Fig. 4d). Accordingly, it is expected that this replacement of SST datasets leads to an increase in the CWV through the enhancement of surface heat fluxes around the coastal region.

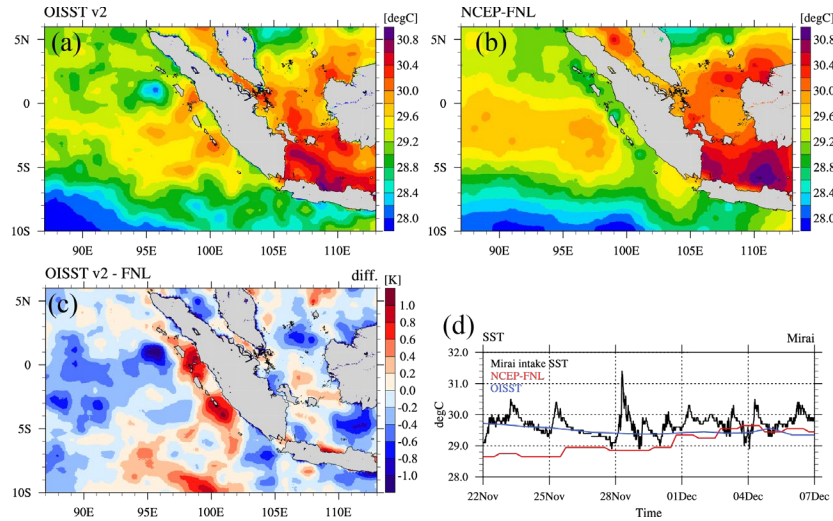


Figure 4: Geographical distributions of OI-SST (a), NCEP-FNL SST (b), and their differences (c) averaged over the simulation period (23 November - 7 December 2015). Panel (d) represents the time series of the observed SST (black) as well as the SSTs analyzed by NCEP-FNL (red) and NOAA (blue) at the stationary observation point of the R/V Mirai.

5. Results of the sensitivity experiments

Five sensitivity experiments are conducted for the purpose of increasing the mean CWV over the ocean (especially around the coastal region), as previously mentioned. The first 3 sensitivity tests (ICE, WW14M, and CLOUD) are primarily concerned with the radiation process, while the latter 2 experiments (NOR10 and SST) are intended to spotlight the surface heat fluxes. Accordingly, those results are separately documented here.

First, we average the terms in Eq. (1) over the simulation period and calculate the anomalies from the control experiment to examine whether each term works positively or negatively in the sensitivity tests. Subsequently, we evaluate the performance of the simulations, focusing on the time-mean precipitation and OLR as well as CWV. Notably, the advection term in Eq. (1) is calculated as a residual of the other terms (radiative heating, surface heat fluxes, and local derivative of the CFMSE), although it can be directly derived from the outputs of the simulation. Temporal and spatial variations in the advection are much noisier than those of radiative heating and surface heat fluxes. In addition, in our simulations, historical files are archived every 1 hour due to the limitation of computer resources, and the accumulated snapshots of the advection terms would contain substantial errors. Therefore, it is likely that such a calculation procedure for the advection mitigates numerical errors, although incompleteness is imposed on the advection.

The three experiments of ICE, WW14M, and CLOUD are all intended to enhance radiative heating. Nevertheless, the results show diversity. In the ICE experiment, positive anomalies of radiative heating are extended over the model domain (Fig. 5a). Larger amounts of ice clouds are simulated in the upper level due to the slower terminal velocity (not shown), which would promote warming effects. In contrast to the ICE experiment, the modifications of the parameters for snow and graupel (WW14M) and smaller effective radius of water clouds (CLOUD) have negative and negligible (or slightly negative) impacts on radiative heating, respectively (Figs. 5b and 5c). In addition, surface fluxes follow radiation effects, which are slightly enhanced in the ICE experiment

(Fig. 5d), while negative anomalies prevail in the WW14M (Fig. 5e), and few changes are found over the ocean in the CLOUD experiment (Fig. 5f). Interestingly, advection counteracts the source terms in all the experiments (Figs. 5g, 5h and 5i). However, contributions of the source terms generally exceed those of the advection. As a result, the time-mean CWV (or CFMSE) increases in the ICE experiment (Fig. 6a), decreases in the WW14M experiment (Fig. 6b) and is subtly reduced in the CLOUD experiment (Fig. 6c).

Reflecting the CWV changes, positive anomalies of precipitation are found around the western coastal region in the ICE experiment (Fig. 6d). More importantly, the seaside peak in rainfall becomes more noticeable in the ICE experiment, although it is still insufficient in comparison with the satellite-retrieved precipitation. In addition, the positive biases of OLR are considerably reduced over the entire domain in the ICE experiment (Fig. 6g). Negative anomalies of precipitation are dominant in the WW14M experiment (Fig. 6e), and changes are hardly seen in the CLOUD experiment (Fig. 6f), which also agrees with the CWV anomalies. In contrast to the ICE experiment, positive OLR biases are still extended over the domain (especially prominent around the western coast of Sumatra Island) in these experiments (Figs. 6h and 6i). These results indicate that the simulation fidelity is improved by the smaller particle size of the ice cloud (ICE) and degraded by the dominance of snow and graupel (WW14M), while the optical thickness of water clouds is irrelevant to the model performance overall (CLOUD), at least in the present experimental framework.

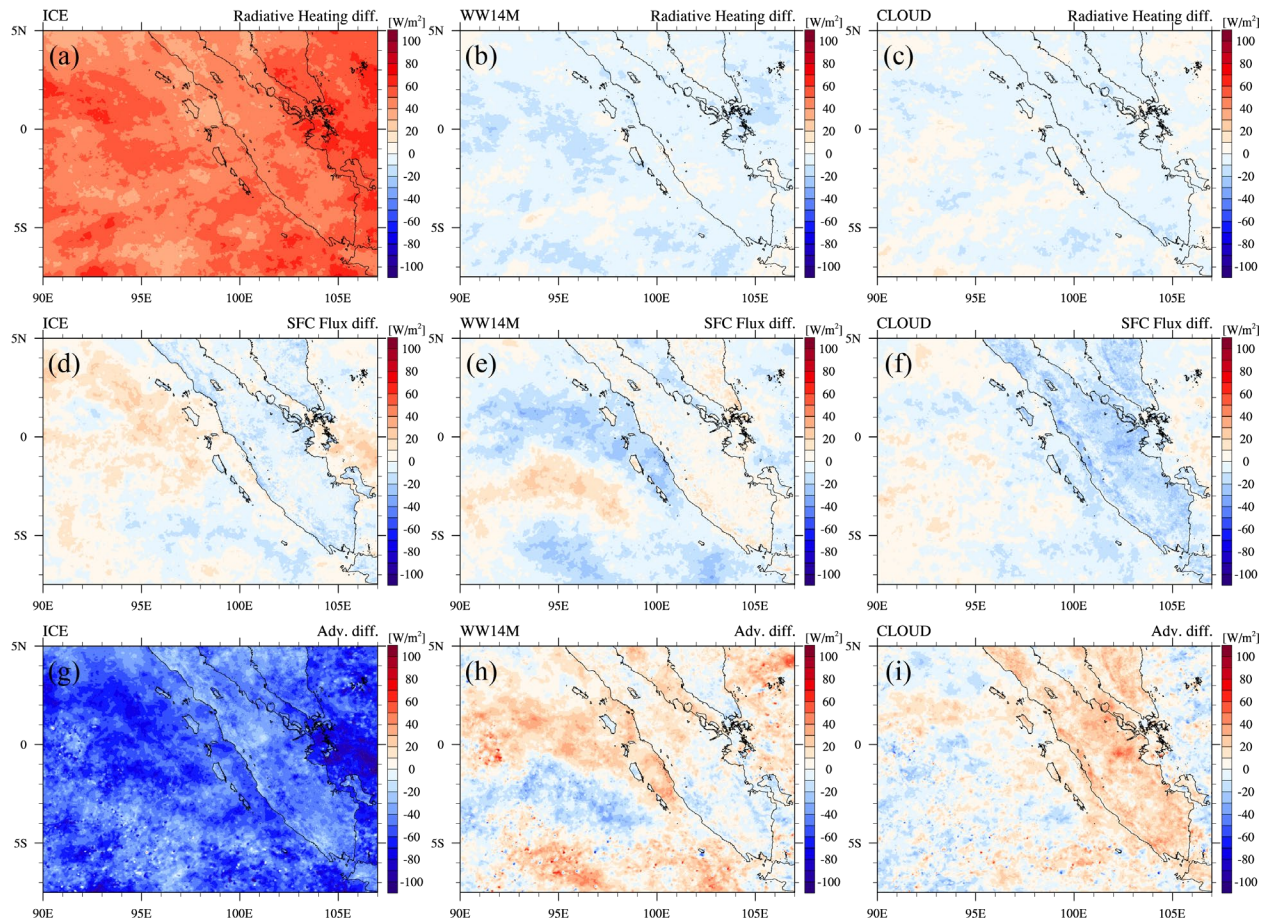


Figure 5: Anomalies of the column-integrated radiative heating (top), surface heat flux (middle), and FMSE advection (bottom) averaged over the simulation period in the ICE (left), WW14M (center), and CLOUD (right) experiments. The results in the control experiment are subtracted to obtain the anomaly.

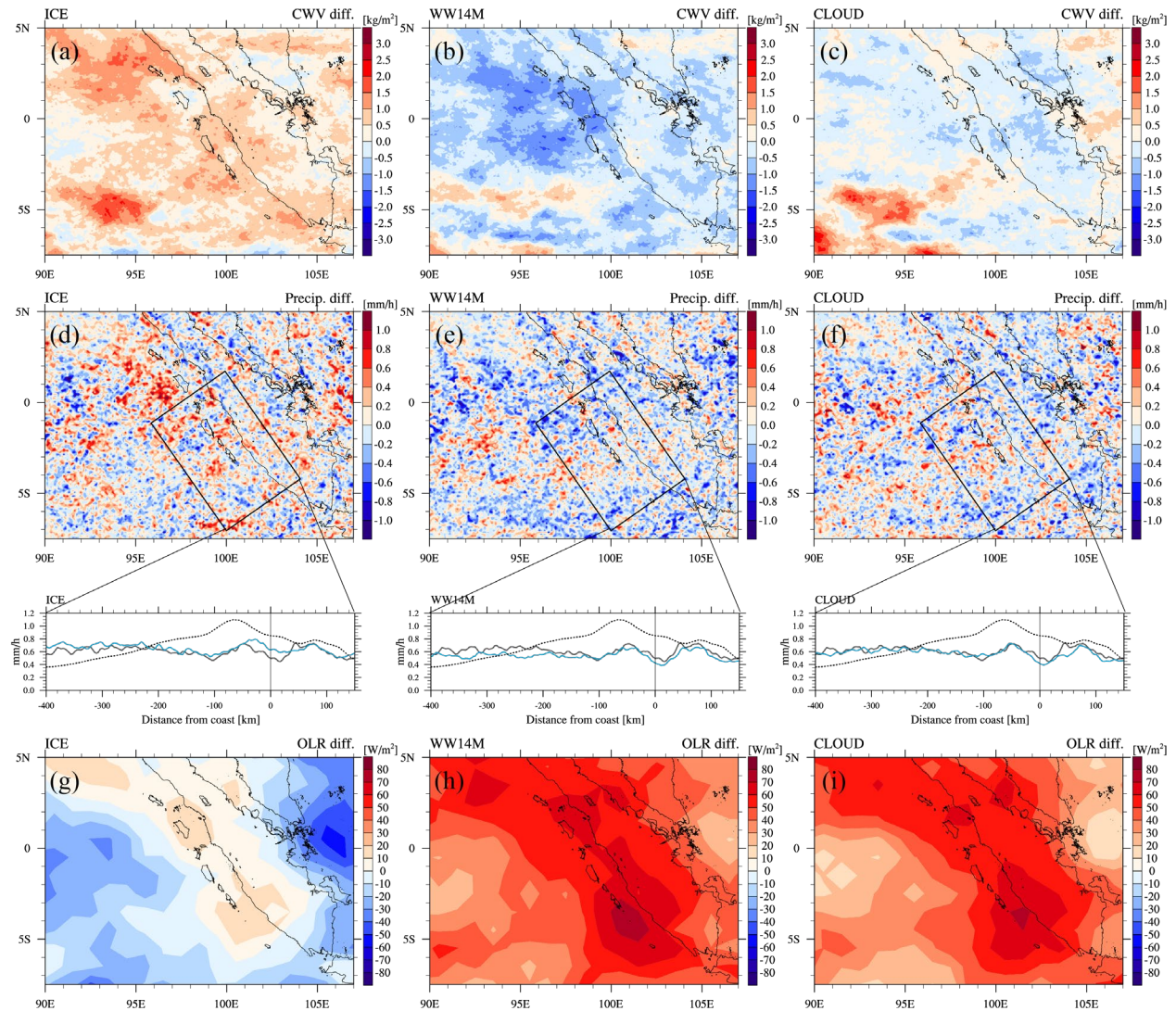


Figure 6: Same as in Fig. 5 but for CWV (top), precipitation (middle) and OLR (bottom). Lower panels in the middle represent rainfall distributions expressed by a function of the distance from the western edge of Sumatra Island (blue solid line) over the rectangular area in (d), (e) and (f) in each sensitivity test, as well as in the control (black solid line) and satellite retrieval (black dashed line).

Impacts on the surface heat fluxes are primarily tested in the NOR10 and SST experiments. Positive anomalies of the fluxes are represented over the ocean in the NOR10 experiment (Fig. 7c). Horizontal winds are intensified in the lower level, in association with promoted evaporation of

rainwater in the N0R10 experiment (not shown), and the strong surface wind would be responsible for the flux enhancement. In the SST experiment, the fluxes are enhanced and reduced in the coastal region and open ocean, respectively (Fig. 7d), which reflects the replaced SST distributions in the control and SST experiments (NCEP-FNL SST vs. NOAA OI-SST; Fig. 4). It is also found that radiative heating basically follows the surface flux changes (Figs. 7a and 7b) and that advection tends to cancel the effects of the source terms (Figs. 7e and 7f).

The positive anomalies of the source terms in the N0R10 experiment lead to an increase in the time-mean CWV (Fig. 8a), and more rainfall is brought over the coastal area as well as over the open ocean (Fig. 8c). However, the coastal peak in precipitation becomes obscure due to excessive rainfall over the ocean. In the SST experiment, the time-mean CWV decreases over the open ocean (Fig. 8b), in association with the weakened source term in Eq. (1). On the other hand, positive anomalies of CWV and rainfall are located around the southwestern coast of Sumatra Island, corresponding with the warmer SST in this region (Figs. 8b and 8d). As a result, the decreasing trend of rainfall toward the offshore region is better reproduced in the SST experiment (Fig. 8d). Notably, the N0R10 and SST experiments still suffer from the positive biases of OLR (Figs. 8e and 8f), and the radiation fields show no remarkable improvements.

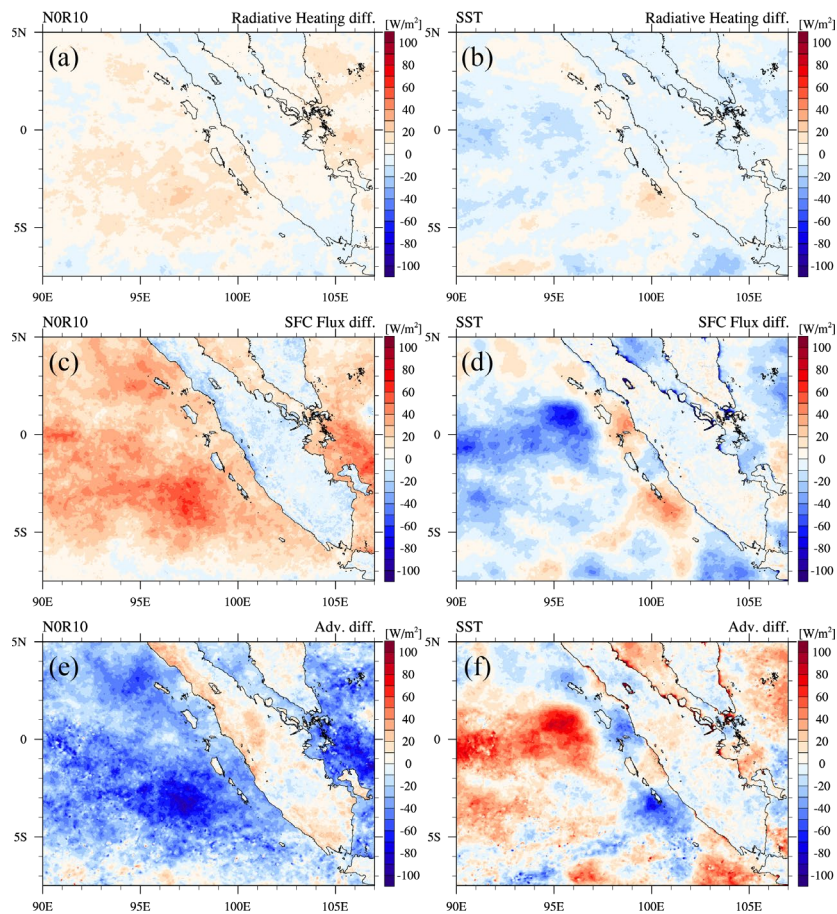


Figure 7: Same as in Fig. 5 but for the N0R10 (left) and SST (right) experiments.

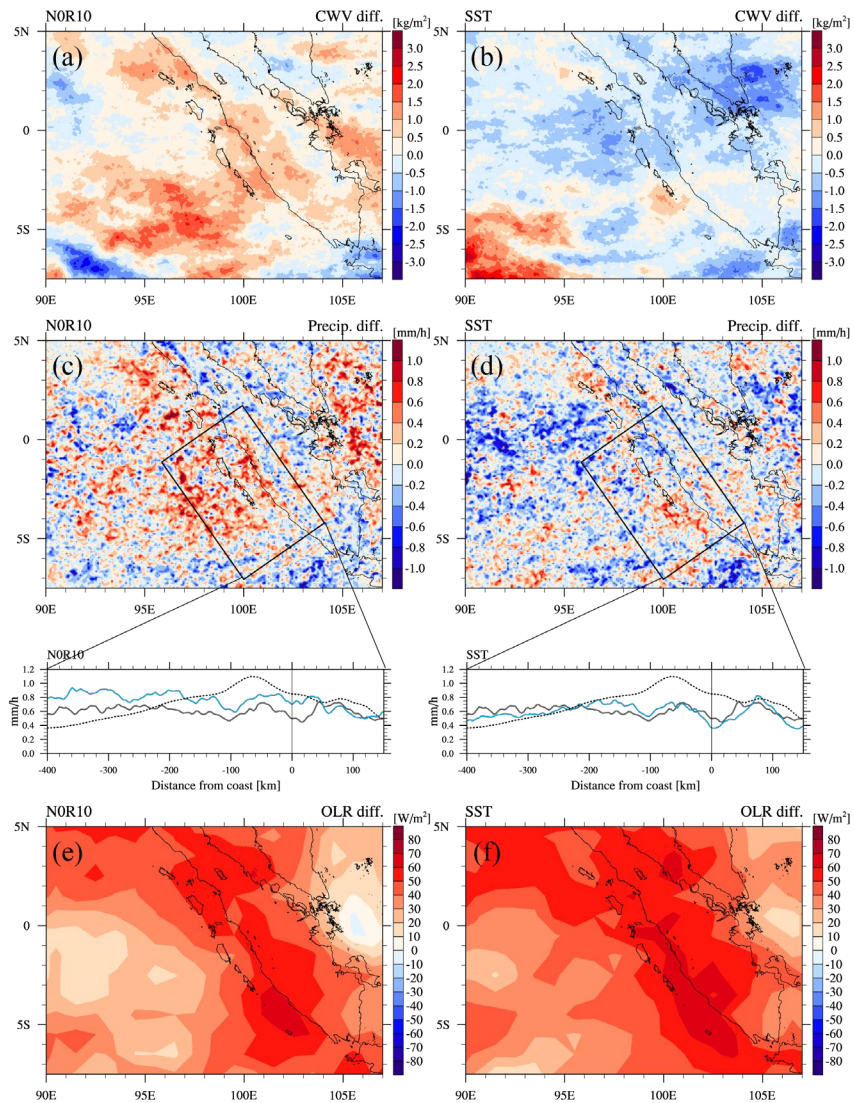


Figure 8: Same as in Fig. 6 but for the NOR10 (left) and SST (right) experiments.

When the results of the five sensitivity experiments are synthesized, increases in the CWV and associated precipitation over the ocean are reproduced in the ICE, NOR10, and SST experiments (not in the WW14M and CLOUD experiments). However, the improvements are modest, and it would be fair to say that the precipitation concentration around the coastal sea area is unsatisfactorily simulated in these experiments. On the other hand, different features of the simulations suggest that the combination of these experiments might complementarily achieve more progress, especially in terms of the precipitation concentration around the coastal area. Therefore, we conduct additional three sensitivity tests using the experiments of ICE, NOR10, and SST, which are named ICE+NOR10, ICE+SST, and SST+NOR10 experiments, respectively. For example, in the ICE+NOR10 experiment, the parameterizations of ice clouds and rain are both modified, following the procedures of the ICE and NOR10 experiments.

The results of these combination experiments exhibit the general features of single sensitivity tests; inclusion of the modified ice cloud parameterization leads to reinforcement of radiative heating (Figs. 9a, 9b, and 9c). Similarly, OI-SST products enhance the contrast of the surface heat fluxes between the coastal region and open ocean, such as the SST experiment (Figs. 9d, 9e, and 9f), and advection counteracts source terms (Figs. 9g, 9h, and 9i). However, the anomalies from the control experiment are more emphasized in these combination experiments. As a result, the time-mean CWV and precipitation are much larger over the ocean in these experiments (Figs. 10). More importantly, the ICE+SST experiment represents a prominent peak in the precipitation around the coastal sea area, while excessive rainfall over the ocean makes the peak obscure in the experiments including NOR10 (ICE+NOR10 and SST+NOR10). Furthermore, OLR biases are minimized in the ICE+SST experiment. Therefore, it is concluded that the cloud ice parameterization and SST distributions are crucial for the better fidelity of coastline rainfall concentration, at least in the present experimental designs. Finally, it should also be emphasized here that more smoothed distributions of CWV and general agreements between CWV and precipitation show the advantage of focusing on the CWV (or CFMSE) budget equation in the present investigation.

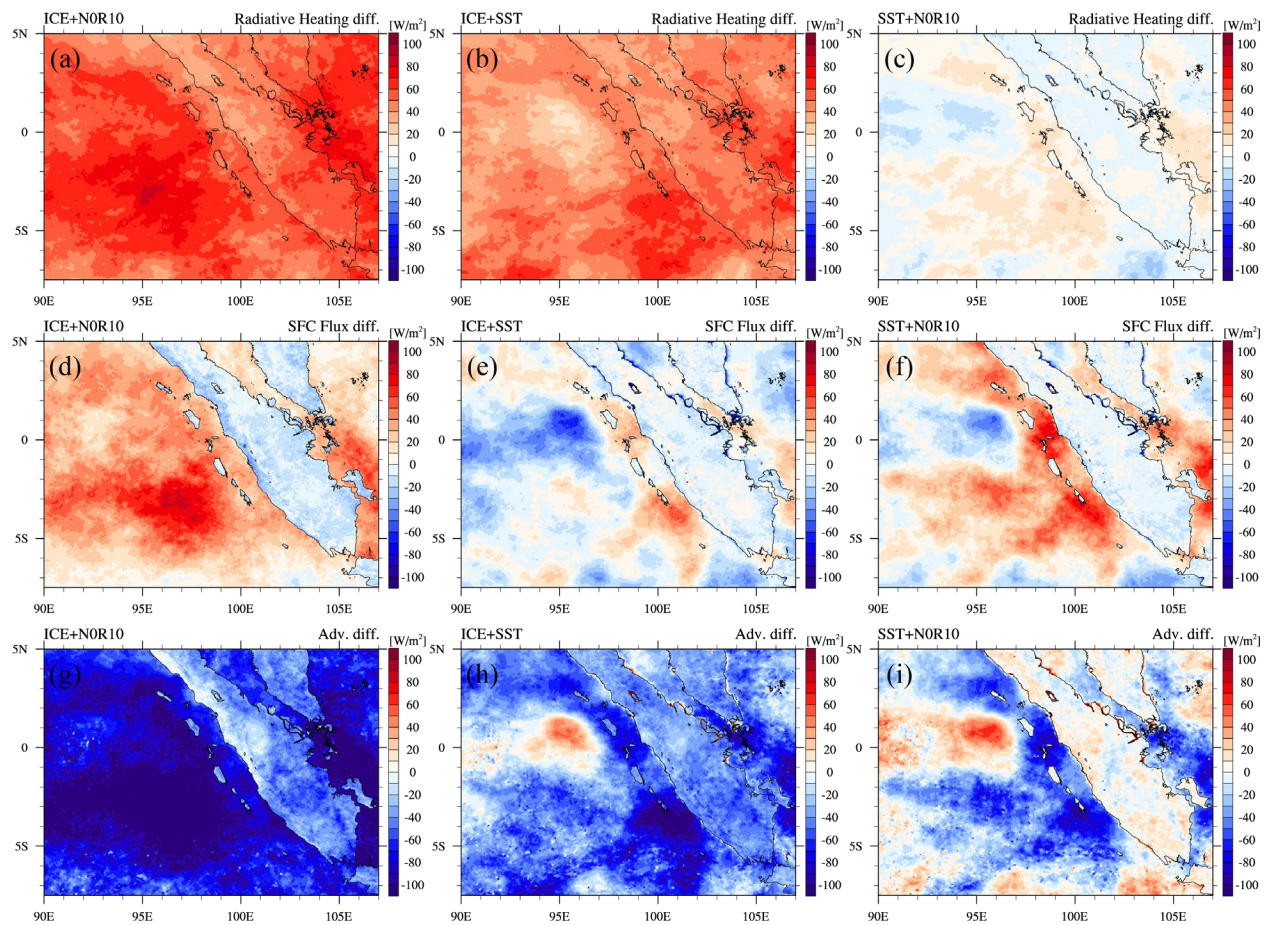


Figure 9: Same as in Fig. 5 but for the ICE+NOR10 (left), ICE+SST (center), and SST+NOR10 (right) experiments.

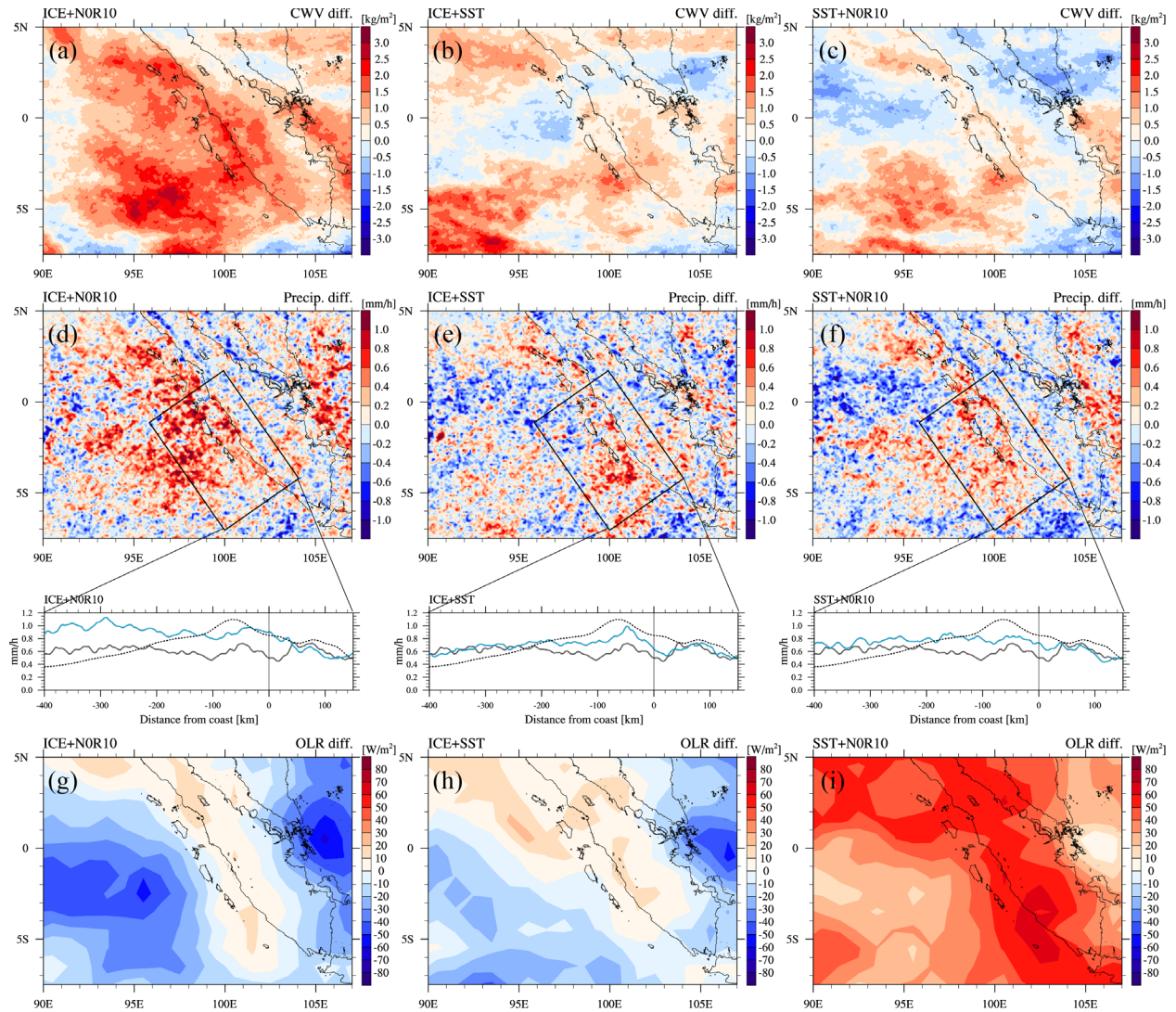


Figure 10: Same as in Fig. 6 but for the ICE+N0R10 (left), ICE+SST (center), and SST+N0R10 (right) experiments.

6. Diurnal cycle and precipitation peak over the coastal seaside region

In the previous sections, we evaluated model performances based on the CFMSE budget equation. Under the WTG assumption, sub-daily variations should be filtered out, and thus, the CFMSE evolution is practically equivalent to that of CWV. However, coastal rainfall is significantly affected by convective systems over land with a prominent diurnal cycle, as reviewed in the introduction. Accordingly, one might claim that the better fidelity of the precipitation peak is achieved at the expense of performances on the diurnal rainfall cycle in the ICE+SST experiment. Conversely, it is also possible that the diurnal rainfall variations are better reproduced in the ICE+SST experiment in association with the time-mean rainfall. Therefore, in the present section, the fidelity of the diurnal cycle is briefly described, comparing the results obtained in the control and ICE+SST experiments with in situ observations in the Pre-YMC campaign.

Radiosonde soundings at Bengkulu indicate that the sea breeze begins to evolve at approximately 10 LT near the surface (Fig. 11a). The layers with positive (inland-ward) horizontal winds gradually deepen and reach 2 km in height at approximately 16 LT. After 16 LT, land breezes appear near the surface, and the negative (offshore-ward) horizontal wind is intensified in the evening. Corresponding with the wind variations, precipitation is initiated over the land at approximately 14 LT (Fig. 11d). After the development of convection, the main precipitation areas move to the west and redevelop over the coastal region, while eastward migrating signals are weak. The speed of the westward migration of the precipitating area is $3\text{--}7\text{ m s}^{-1}$, which agrees with the estimates from surface observations (e.g., Yokoi et al., 2017).

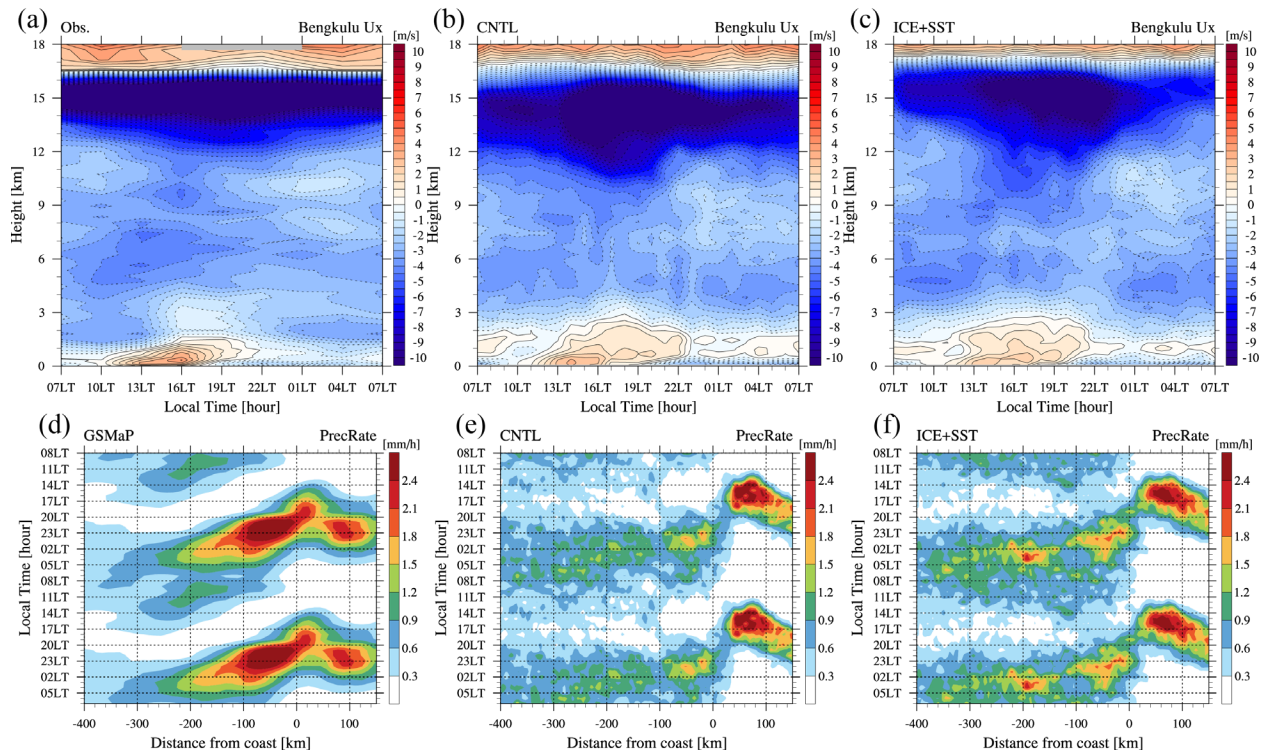


Figure 11: (Upper) Composite diurnal variations in the southwest–northeast component (perpendicular to the coastline) of the horizontal wind derived from radiosonde soundings (a) and calculated in the control (b) and ICE+SST (c) experiments at the Bengkulu observatory. (Lower) Composite diurnal cycle of precipitation retrieved from satellite observations (d) and simulated by the control (b) and ICE+SST (c) experiments in the rectangular areas in Figs. 2a, 2d, and 10e. While the abscissa and ordinate in the upper panels indicate local time and height, respectively, those in the lower panels represent the distance from the western edge of Sumatra Island and local time, respectively.

The control and ICE+SST experiments also show that the sea breeze evolves at approximately 10 LT (Figs. 11b and 11c). However, the depth of the circulation exceeds 2 km in height (close to 3 km), and the retreat signals are obscure, which is in contrast to the observations. In terms of the diurnal cycle of precipitation, convection initially appears around the elevated orography, and the time of development (approximately 12 LT) is earlier than that of the satellite

retrievals (Figs. 11e and 11f). Furthermore, the precipitation systems predominantly move to the east in the simulations. However, westward migration signals are still recognized in both experiments, and the moving speed is estimated to be $1.5\text{--}4.5\text{ m s}^{-1}$, which is slightly slower than that in satellite retrievals ($3\text{--}7\text{ m s}^{-1}$).

Notably, the precipitation systems redevelop around $0\sim -100\text{ km}$ from the coastline in both experiments, although the time-mean precipitation is insufficiently concentrated around the coastal seaside region in the control experiment (Fig. 2d). These results imply that the better fidelity of the seaside precipitation peak in the ICE+SST experiment is irrelevant to that of the rainfall diurnal cycle, which is consistent with the findings obtained in previous studies, as reviewed in the introduction. In fact, most of the sensitivity tests reproduce the redevelopment of convection without conspicuous maxima of the time-mean precipitation over the coastal region (not shown). Namely, more abundant moisture available to precipitation would be essential to the concentrations of the time-mean rainfall over the coastal region in the ICE+SST experiment.

7. Why does the ICE+SST experiment represent better fidelity?

The terminal velocity and effective radius of ice clouds are reduced in the ICE and ICE+SST experiments. Reflecting the modification of the ice cloud parameterization, larger amounts of ice clouds are distributed around the 11-16 km height (Figs. 12a and 12b), and anomalous heating of the radiation is extended at the corresponding altitude (Figs. 12d and 12e). Under the WTG assumption, upward vertical winds are induced to keep the temperature profiles unchanged against radiative heating. In fact, positive anomalies of the vertical winds are found at heights of 6-15 km (Figs. 12g and 12h). In addition, the vertical winds diagnostically estimated from the temperature and radiative heating profiles through the WTG assumption generally agree with the actual vertical wind anomaly in the ICE experiment (Fig. 13b). Positive anomalies of the vertical wind are also located over the warmer SST in the SST experiment (Fig. 12i). Since differences in the ice cloud amounts and radiative heating between the control and SST experiments are subtle (Figs. 12c and 12f), it would be the direct response of the warmer SST imposed on the SST experiment. While the vertical wind anomalies in the ICE+SST experiment are larger in the mid-level than the diagnosed updrafts (Fig. 13a), it is interesting that the linear combination of the vertical wind anomalies in the ICE and SST experiments is able to account for those in the ICE+SST experiment (Fig. 13c) despite their inherent feedback processes.

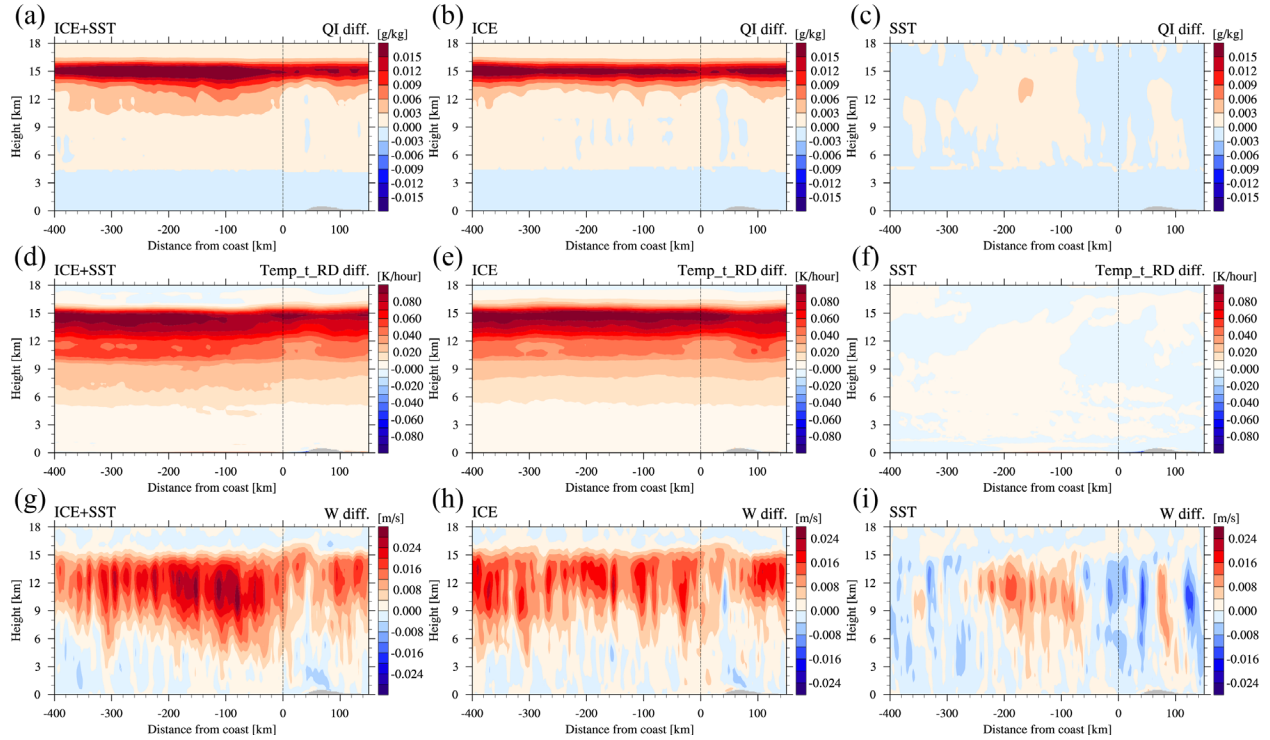


Figure 12: Anomalies of the ice cloud mixing ratio (top), radiative heating (middle), and vertical wind (bottom) averaged over the simulation period in the ICE+SST (left), ICE (center), and SST (right) experiments in the rectangular areas in Figs. 10e, 6d and 8d. The mean profiles in the control experiment are subtracted to obtain the anomaly. The abscissa and ordinate indicate the distance from the western edge of Sumatra Island and height, respectively.

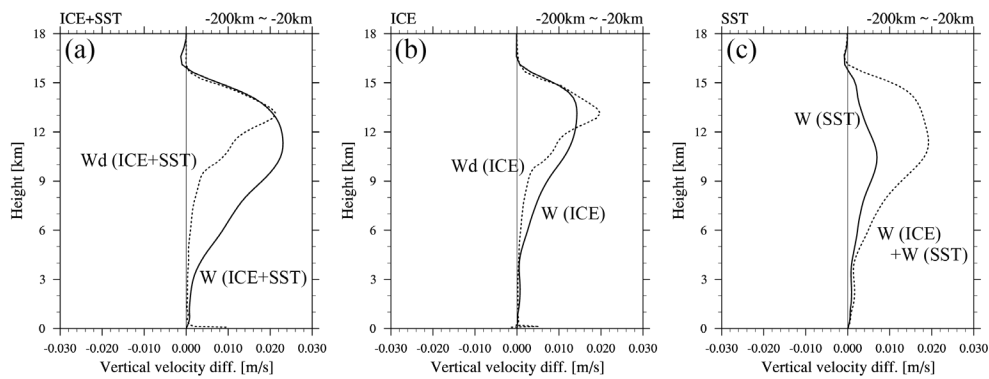


Figure 13: Vertical wind anomalies averaged over the coastal oceanic regions (between -20 km and -200 km distances from the coastline in Figs. 12g, 12h, and 12i) in the ICE+SST (left), ICE (center), and SST (right) experiments. While solid lines represent the anomalies of the actual vertical wind, dashed lines in (a) and (b) indicate the anomalies of the vertical wind diagnosed by keeping the temperature profiles unchanged against the radiative heating, and a dashed line in (c) is a combination of the solid lines in (b) and (c). The corresponding profiles in the control experiment are subtracted to obtain the anomaly.

The enhanced vertical winds are expected to transport more water vapor to the upper level. Positive anomalies of the vertical moisture advection are actually simulated around the 6-11 km height in the ICE+SST experiment (Fig. 14a), which are exclusively accounted for by those of the vertical wind (not shown). In addition, the horizontal moisture advection shows slightly negative anomalies (Figs. 14b). Therefore, it is suggested that the enhanced vertical winds (Figs. 12g) are primarily responsible for the larger amounts of water vapor around the 6-11 km height (Figs. 14c), which results in the larger amounts of CWV around the coastal area (Fig. 10b).

In summary, due to the reduced terminal velocity and effective radius of ice clouds, radiative cooling is inhibited in the ICE and ICE+SST experiments, and anomalous upward vertical wind is intensified to maintain the temperature profile under the WTG assumption. The warmer SST around the coastal region also assists the intensification of the updraft in the SST and ICE+SST experiments. In association with the enhancement of the updrafts, CWV increases through the vertical moisture advection, and thus, more precipitation is brought about. It is considered that these combinations of ICE and SST experiments lead to better fidelity of the seaside rainfall peaks around the coastal area in the ICE+SST experiment.

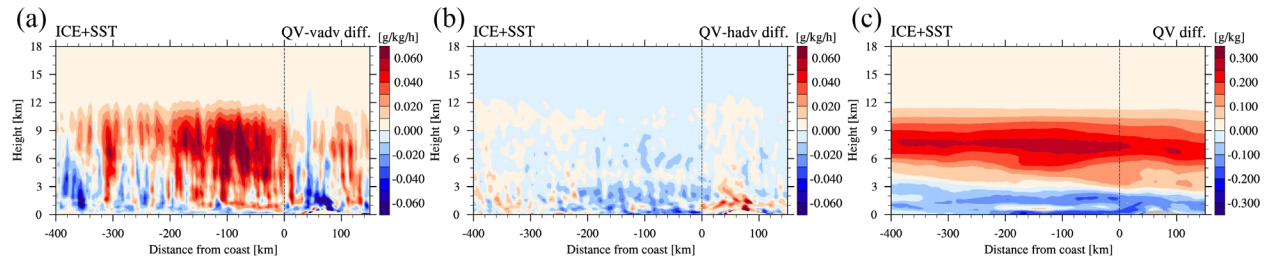


Figure 14: Anomalies of vertical moisture advection (left), horizontal moisture advection (center), and vapor mixing ratio (right) averaged over the simulation period in the ICE+SST in the rectangular areas in Fig. 10e. The mean profiles in the control experiment are subtracted to obtain the anomaly. The abscissa and ordinate indicate the distance from the western edge of Sumatra Island and height, respectively.

The results in the SST and ICE+SST experiments indicate that although the climatologically warmer SSTs along the coast (e.g., Fig. 1b) would be important to the precipitation concentration there, the warmer SST is solely insufficient to account for this concentration. However, the observed SST variations show a prominent diurnal cycle, and the min-to-max range sometimes exceeds 1 K during the simulation period (Fig. 4d). Correspondingly, it is observed that surface heat fluxes are intensified and that more moisture is provided to the atmosphere before the precipitation peak (e.g., Yokoi, 2020). On the other hand, SST variations within the daily time-scale are completely ignored in the ICE+SST and SST experiments, although the analyzed SST used in the control experiment also shows little diurnal cycle (e.g., Fig. 4a). Therefore, the surface heat fluxes would still be underestimated in the ICE+SST and SST experiments. In other words, it is highly likely that combined with the climatologically warmer SSTs, the prominent SST diurnal cycle and the associated enhancement of the heat fluxes in the daytime significantly contribute to the precipitation peak along the western coast of Sumatra Island. These effects of the SST diurnal cycle should be clarified in future studies.

From the reduced biases of the OLR and better fidelity in the ICE and ICE+SST experiments, it is reasonable to consider that the upper-level ice clouds play a role in the precipitation concentration over the coastal seaside region through radiation processes. To highlight the effects of ice clouds, the diurnal cycle in the ICE experiment is elucidated here. Positive anomalies of the radiation and vertical wind are extended over the ocean for a whole day, although patterns of the latter are much noisier than those of the former due to the more localized nature of the vertical wind (Figs. 15a and 15b). Furthermore, closer views of the diurnal cycle reveal that there are two maxima at approximately 20 LT and 05 LT over the coastal region (within 100 km distances from the coastline) in the radiative heating anomalies, and the vertical winds are slightly intensified around that time. Namely, variations in the vertical wind in the upper level generally agree with those of the radiative heating over the coastal oceanic region within the daily time scale. It might be possible that updrafts enhanced by other external forcings cause anomalous radiative heating. However, based on the diagnosis in the time-mean fields shown in Figs. 12, 13 and 14, the general agreements between the updraft and radiative heating variations would indicate that the WTG framework is still valid in the (at least qualitative) discussions within the daily time-scale, although temperature perturbations are not necessarily small. The radiation anomalies are largely accounted for by the OLR anomalies (Fig. 15c), which are directly related to the cloud fields. Therefore, the diurnal variations in OLR and condensates and the associated moisture evolutions in the ICE experiment are examined in the rest of the section.

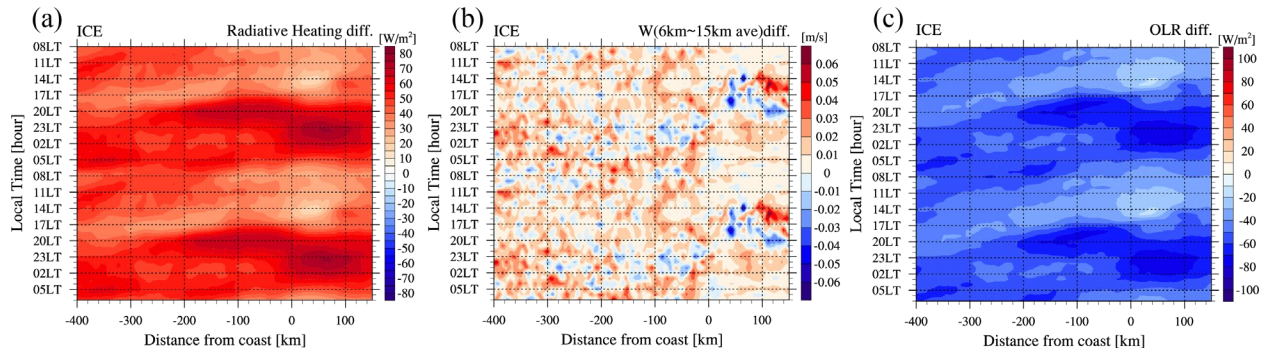


Figure 15: Composite diurnal cycle of the anomalies of radiative heating (a), vertical wind averaged in the 6–15 km height (b), and OLR (c) in the ICE experiment. The diurnal cycles in the control experiment are subtracted to obtain the anomaly. The abscissa and ordinate in the panels indicate the distance from the western edge of Sumatra Island and local time, respectively.

OLR starts to drastically decrease at approximately 17 LT (Fig. 16a), and after reaching a minimum at approximately 20 LT, lower values of the OLR last until dawn (05 LT), with westward shifting over the coastal area (within 100 km distances from the coast). Associated with the OLR variations, the diurnal cycle of the vertically integrated ice clouds shows two peaks, in the evening and at night-predawn (Fig. 16b). In contrast, precipitation peaks at approximately 23 LT–05 LT over the corresponding area (Fig. 16c) and variations in the other condensates (e.g., snow, graupel, and rain water) generally follow those of precipitation (not shown). Accordingly, although the lower OLR and larger ice clouds at night-predawn can be explained by active convection, it does not seem that the evening OLR minimum and ice cloud maximum accompanied by little precipitation are rooted in convection over the coastal area. Furthermore, it is also found that the

areas with larger ice clouds and lower OLR over the land gradually migrate toward the ocean in the afternoon and evening. The migration speed is estimated to be approximately 9 m s^{-1} , which is comparable with the upper-level zonal winds (e.g., Fig. 11). These results and snapshots of the composite diurnal cycle (not shown) suggest that larger amounts of ice clouds and the associated lower OLR at approximately 17 LT- 20 LT originate (or are advected) from inland convection. It should also be noted that moisture accumulation in the middle and lower levels starts at the corresponding time over the coastal area (Fig. 16d). Therefore, in the same way as in Figs. 12, 13 and 14, it is speculated that inland convection, which is strictly regulated by solar insolation, exports ice clouds to the coastal region through upper-level easterly winds, and weakened radiative cooling and intensified updraft assist preconditioning for convection development, leading to more precipitation there. Observations by Mie-scattering lidar on board R/V Mirai exhibit the emergence of upper-level clouds at approximately 16 LT, which is earlier than the arrival of precipitation (e.g., Fig. 7 of Yokoi et al. 2017), and radiosonde soundings show that increases in upper-level moisture predate those in the lower level (Fig. 17a), which is reproduced well in the ICE experiment (Fig. 17b) and consistent with our speculation.

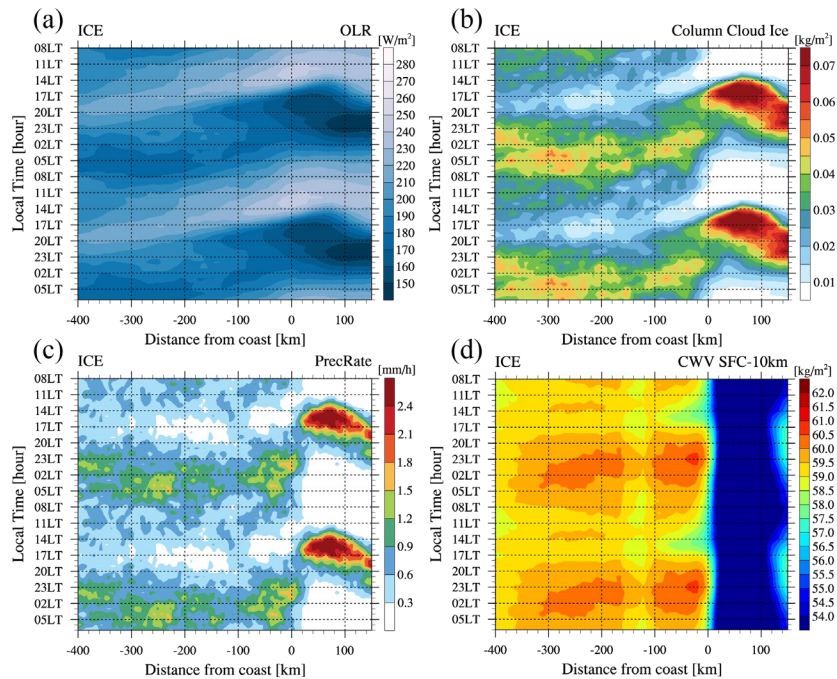


Figure 16: Same as in Fig. 15 but for the composite diurnal cycle of OLR (a), column-integrated ice cloud (b), precipitation (c), and CWV in the lower level (lower than 10 km in height) (d) in the ICE experiment.

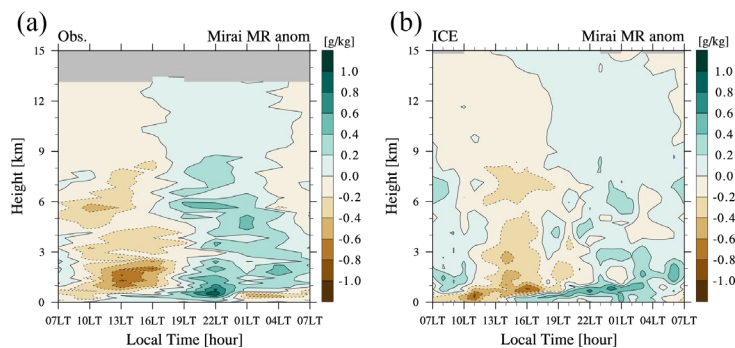


Figure 17: Composite diurnal variations in the vapor mixing ratio derived from radiosonde soundings (a) and calculated in the ICE experiment (b) at the stationary observation point of the R/V Mirai. In the panels, the abscissa and ordinate indicate the local time and height, respectively, and the time-mean profiles are subtracted to emphasize the diurnal cycle.

The easterly wind almost persistently prevails in the upper troposphere over the MC, and ice clouds are expected to be provided over the coastal region from inland convection throughout the year. In fact, Yanase et al. (2017) found that stratiform-dominated rainfall exclusively propagates westward, corresponding with the easterly background wind in the mid-upper troposphere, although convective-dominated rainfall migrates to the east or west in association with the lower-level tropospheric wind. These observational findings also support our speculations. Moreover, the mechanism proposed here seems to be relevant to the fact that the seaside precipitation peak is especially prominent along the western coast in other regions (e.g., Indochina Peninsula), while rainfall concentrations are weak along the northern, southern, and eastern coasts over the MC, as reviewed in the introduction. Further investigations are required to elucidate the role of ice clouds in seaside rainfall peaks along the coastline.

8. Summary and conclusions

Satellite observations have documented that significant amounts of precipitation are concentrated in coastal areas in the tropics (e.g., Ogino et al. 2016). The rainfall concentration is remarkable around the western coast of Sumatra Island, which is known as one of the regions with the largest climatological precipitation. However, the mechanism remains unclear. Furthermore, most of the models, which include a cloud(-system)-resolving model, as well as a general circulation model with convective parameterization, fail to reproduce the precipitation concentration, although the diurnal cycle is more adequately simulated over the MC. Therefore, in the present study, numerical experiments were conducted, with a focus on precipitation patterns off the coast of Sumatra Island. The integrations started on 22 November 2015 and ended on 7 December 2015, which corresponded to the intensive observational period of the Pre-YMC campaign.

In the control experiment, the rainfall concentration along the western coast of Sumatra Island was obscure, although the small peak in the precipitation was located, and dry biases were found in the corresponding region. Precipitation is monotonically dependent on CWV over tropical coastal areas, as well as over the open ocean. In addition, under the WTG approximation, the evolution of CFMSE is nearly equivalent to CWV. Therefore, the present investigation used the CFMSE budget equation to formulate sensitivity experiments, and 6 sensitivity experiments were

conducted, in which the terminal velocity and effective radius of ice clouds were reduced (ICE), intercept parameters of snow and graupel were increased (WW14M), the effective radius of cloud droplets were downsized (CLOUD), the intercept parameter of rain was increased by ten times (N0R10), and SST data were replaced with OI-SST datasets provided by NOAA.

Increases in the CWV and associated precipitation over the ocean were simulated in the ICE, N0R10, and SST experiments, although the WW14M and CLOUD experiments did not show any improvements. However, the precipitation concentration around the coastal seaside region was insufficiently reproduced even in the ICE, N0R10, and SST experiments. Therefore, additional 3 sensitivity tests were conducted by selecting the two experiments of ICE, N0R10, and SST (ICE+N0R10, ICE+SST, and SST+N0R10). While the results of these combination experiments showed the general features of single sensitivity tests, the enhancement of CWV and precipitation around the coastal sea area were well simulated in the ICE+SST experiment. Diagnosis in the time-mean fields in the ICE+SST experiment indicated that due to the inhibition of radiative cooling and warmer SSTs, the anomalous upward vertical wind was induced and CWV and precipitation increased through the enhancement of the vertical moisture advection over the coastal region.

It has been pointed out that the development of coastal convection is significantly affected by convective systems over land with a prominent diurnal cycle. Although the time-mean precipitation is insufficiently concentrated around the coastal seaside region in the simulations, except for the ICE+SST experiment, there are subtle differences in the diurnal cycle of precipitation among the experiments. Accordingly, the better fidelity of the seaside precipitation peak is irrelevant to that of the precipitation diurnal cycle over the coastal region.

Comparing the simulation results with the in situ observations, we speculated that in addition to the climatologically warmer SSTs, the prominent SST diurnal cycle and the associated enhancement of the heat fluxes in the daytime significantly contribute to the precipitation peak along the western coast of Sumatra Island. Furthermore, the lateral transport of ice clouds from Sumatra Island to the ocean, which is associated with the strong diurnal cycle of inland convection, contributes to the concentration of precipitation along the coastal region. These speculations were consistent with the observed diurnal variations in upper-level clouds and moisture and might be relevant to the fact that the seaside precipitation peak is more prominent along the western coast than the northern, southern, and eastern coasts over the MC. Further investigations are required to clarify the roles of the SST diurnal cycle and upper-level ice clouds.

Acknowledgments

Numerical simulations were conducted by using ver. 5.2.5 of the Scalable Computing for Advanced Library Environment-Regional Model (SCALE-RM), and the authors are grateful to all those who were engaged in the development of SCALE-RM. To evaluate the model performances, following datasets were used; in situ observations during the Pre-YMC field campaign (by the Japan Agency for Marine–Earth Science and Technology (JAMSTEC), the Indonesian Agency for the Assessment and Application of Technology (BPPT), and the Indonesian Agency for Meteorology, Climatology and Geophysics (BMKG)), National Centers for Environmental Prediction Final Operational Global Analysis (NCEP-FNL), Global Satellite Mapping of Precipitation (by Japan Aerospace Exploration Agency (JAXA)), High Resolution SST (by the NOAA/OAR/ESRL PSL, Boulder, Colorado, USA, from their Web site at <https://psl.noaa.gov/>). We would like to express our sincere thanks to all concerned in these products. This work was supported by JSPS KAKENHI Grants JP17H04477 and JP19H05697, and Environment Research

and Technology Development fund (2-1904) of the Environmental Restoration and Conservation Agency of Japan. This study was also supported by the Cooperative Research Activities of Collaborative Use of Computing Facility of the Atmosphere and Ocean Research Institute, the University of Tokyo.

References

- Adames, Á. F., & Kim, D. (2016). The MJO as a Dispersive, Convectively Coupled Moisture Wave: Theory and Observations. *Journal of the Atmospheric Sciences*, *73*(3), 913–941. <https://doi.org/10.1175/JAS-D-15-0170.1>
- Ahmed, F., & Schumacher, C. (2017). Geographical differences in the tropical precipitation-moisture relationship and rain intensity onset. *Geophysical Research Letters*, *44*(2), 1114–1122. <https://doi.org/10.1002/2016GL071980>
- Andersen, J. A., & Kuang, Z. (2011). Moist Static Energy Budget of MJO-like Disturbances in the Atmosphere of a Zonally Symmetric Aquaplanet. *Journal of Climate*, *25*(8), 2782–2804. <https://doi.org/10.1175/JCLI-D-11-00168.1>
- Arakawa, O., & Kitoh, A. (2005). Rainfall Diurnal Variation over the Indonesian Maritime Continent Simulated by 20 km-mesh GCM. *SOLA*, *1*, 109–112. <https://doi.org/10.2151/sola.2005-029>
- Argüeso, D., Romero, R., & Homar, V. (2019). Precipitation Features of the Maritime Continent in Parameterized and Explicit Convection Models. *Journal of Climate*, *33*(6), 2449–2466. <https://doi.org/10.1175/JCLI-D-19-0416.1>
- Baranowski, D. B., Waliser, D. E., Jiang, X., Ridout, J. A., & Flatau, M. K. (2019). Contemporary GCM Fidelity in Representing the Diurnal Cycle of Precipitation Over the Maritime Continent. *Journal of Geophysical Research: Atmospheres*, *124*(2), 747–769. <https://doi.org/10.1029/2018JD029474>
- Bergemann, M., & Jakob, C. (2016). How important is tropospheric humidity for coastal rainfall in the tropics? *Geophysical Research Letters*. John Wiley & Sons, Ltd. <https://doi.org/10.1002/2016GL069255>
- Bergemann, M., Jakob, C., & Lane, T. P. (2015). Global detection and analysis of coastline-associated rainfall using an objective pattern recognition technique. *Journal of Climate*, *28*(18), 7225–7236. <https://doi.org/10.1175/JCLI-D-15-0098.1>
- Bergemann, M., Khouider, B., & Jakob, C. (2017). Coastal Tropical Convection in a Stochastic Modeling Framework. *Journal of Advances in Modeling Earth Systems*, *9*(7), 2561–2582. <https://doi.org/10.1002/2017MS001048>
- Bhatt, B. C., Sobolowski, S., & Higuchi, A. (2016). Simulation of Diurnal Rainfall Variability over the Maritime Continent with a High-Resolution Regional Climate Model. *Journal of the Meteorological Society of Japan. Ser. II*, *94A*, 89–103. <https://doi.org/10.2151/jmsj.2015-052>
- Bretherton, C. S., Peters, M. E., & Back, L. E. (2004). Relationships between Water Vapor Path and Precipitation over the Tropical Oceans. *Journal of Climate*, *17*(7), 1517–1528. [https://doi.org/10.1175/1520-0442\(2004\)017<1517:RBWVPA>2.0.CO;2](https://doi.org/10.1175/1520-0442(2004)017<1517:RBWVPA>2.0.CO;2)
- Chang, C.-P., & Lau, K. M. (1982). Short-Term Planetary-Scale Interactions over the Tropics and Midlatitudes during Northern Winter. Part I: Contrasts between Active and Inactive Periods. *Monthly Weather Review*, *110*(8), 933–946. [https://doi.org/10.1175/1520-0493\(1982\)110<0933:STPSIO>2.0.CO;2](https://doi.org/10.1175/1520-0493(1982)110<0933:STPSIO>2.0.CO;2)

- Chuda, T., Niino, H., Yoneyama, K., Katsumata, M., Ushiyama, T., & Tsukamoto, O. (2008). A Statistical Analysis of Surface Turbulent Heat Flux Enhancements Due to Precipitating Clouds Observed in the Tropical Western Pacific. *Journal of the Meteorological Society of Japan. Ser. II*, 86(3), 439–457. <https://doi.org/10.2151/jmsj.86.439>
- Dai, A. (2001). Global Precipitation and Thunderstorm Frequencies. Part II: Diurnal Variations. *Journal of Climate*, 14(6), 1112–1128. [https://doi.org/10.1175/1520-0442\(2001\)014<1112:GPATFP>2.0.CO;2](https://doi.org/10.1175/1520-0442(2001)014<1112:GPATFP>2.0.CO;2)
- Dipankar, A., Webster, S., Huang, X.-Y., & Doan, V. Q. (2019). Understanding Biases in Simulating the Diurnal Cycle of Convection over the Western Coast of Sumatra: Comparison with Pre-YMC Observation Campaign. *Monthly Weather Review*, 147(5), 1615–1631. <https://doi.org/10.1175/MWR-D-18-0432.1>
- Esbensen, S. K., & McPhaden, M. J. (1996). Enhancement of Tropical Ocean Evaporation and Sensible Heat Flux by Atmospheric Mesoscale Systems. *Journal of Climate*, 9(10), 2307–2325. [https://doi.org/10.1175/1520-0442\(1996\)009<2307:EOTOEA>2.0.CO;2](https://doi.org/10.1175/1520-0442(1996)009<2307:EOTOEA>2.0.CO;2)
- Fujita, M., Yoneyama, K., Mori, S., Nasuno, T., & Satoh, M. (2011). Diurnal Convection Peaks over the Eastern Indian Ocean off Sumatra during Different MJO Phases. *Journal of the Meteorological Society of Japan. Ser. II*, 89A, 317–330. <https://doi.org/10.2151/jmsj.2011-A22>
- Fukao, S. (2006). Coupling Processes in the Equatorial Atmosphere (CPEA): A Project Overview. *Journal of the Meteorological Society of Japan. Ser. II*, 84A, 1–18. <https://doi.org/10.2151/jmsj.84A.1>
- Grossman, R. L., & Durran, D. R. (1984). Interaction of low-level flow with the Western Ghat Mountains and offshore convection in the summer monsoon. *Monthly Weather Review*, 112(4), 652–672. [https://doi.org/10.1175/1520-0493\(1984\)112<0652:IOLLFW>2.0.CO;2](https://doi.org/10.1175/1520-0493(1984)112<0652:IOLLFW>2.0.CO;2)
- Hara, M., Yoshikane, T., Takahashi, H. G., Kimura, F., Noda, A., & Tokioka, T. (2009). Assessment of the Diurnal Cycle of Precipitation over the Maritime Continent Simulated by a 20 km Mesh GCM Using TRMM PR Data. *Journal of the Meteorological Society of Japan*, 87A, 413–424. <https://doi.org/10.2151/jmsj.87A.413>
- Hassim, M. E. E., Lane, T. P., & Grabowski, W. W. (2016). The diurnal cycle of rainfall over New Guinea in convection-permitting WRF simulations. *Atmospheric Chemistry and Physics Discussions*, 15(13), 18327–18363. <https://doi.org/10.5194/acpd-15-18327-2015>
- Heddinghaus, T. R., & Krueger, A. F. (1981). Annual and Interannual Variations in Outgoing Longwave Radiation over the Tropics. *Monthly Weather Review*, 109(6), 1208–1218. [https://doi.org/10.1175/1520-0493\(1981\)109<1208:AAIVIO>2.0.CO;2](https://doi.org/10.1175/1520-0493(1981)109<1208:AAIVIO>2.0.CO;2)
- Hendon, H. H., & Woodberry, K. (1993). The diurnal cycle of tropical convection. *Journal of Geophysical Research: Atmospheres*, 98(D9), 16623–16637. <https://doi.org/10.1029/93JD00525>
- Heymsfield, A. J., & Donner, L. J. (1990). A Scheme for Parameterizing Ice-Cloud Water Content in General Circulation Models. *Journal of the Atmospheric Sciences*, 47(15), 1865–1877. [https://doi.org/10.1175/1520-0469\(1990\)047<1865:ASFPIC>2.0.CO;2](https://doi.org/10.1175/1520-0469(1990)047<1865:ASFPIC>2.0.CO;2)

- Heymsfield, A. J., van Zadelhoff, G.-J., Donovan, D. P., Fabry, F., Hogan, R. J., & Illingworth, A. J. (2007). Refinements to Ice Particle Mass Dimensional and Terminal Velocity Relationships for Ice Clouds. Part II: Evaluation and Parameterizations of Ensemble Ice Particle Sedimentation Velocities. *Journal of the Atmospheric Sciences*, *64*(4), 1068–1088. <https://doi.org/10.1175/JAS3900.1>
- Holloway, C. E., & Neelin, J. D. (2009). Temporal Relations of Column Water Vapor and Tropical Precipitation. *Journal of the Atmospheric Sciences*, *67*(4), 1091–1105. <https://doi.org/10.1175/2009JAS3284.1>
- Houze Jr., R. A. (2004). Mesoscale convective systems. *Reviews of Geophysics*, *42*(4). <https://doi.org/10.1029/2004RG000150>
- Houze, R. A. (1997). Stratiform Precipitation in Regions of Convection: A Meteorological Paradox? *Bulletin of the American Meteorological Society*, *78*(10), 2179–2196. [https://doi.org/10.1175/1520-0477\(1997\)078<2179:SPIROC>2.0.CO;2](https://doi.org/10.1175/1520-0477(1997)078<2179:SPIROC>2.0.CO;2)
- Houze, R. A., Geotis, S. G., Marks, F. D., & West, A. K. (1981). Winter Monsoon Convection in the Vicinity of North Borneo. Part I: Structure and Time Variation of the Clouds and Precipitation. *Monthly Weather Review*, *109*(8), 1595–1614. [https://doi.org/10.1175/1520-0493\(1981\)109<1595:WMCITV>2.0.CO;2](https://doi.org/10.1175/1520-0493(1981)109<1595:WMCITV>2.0.CO;2)
- Ichikawa, H., & Yasunari, T. (2006). Time-space characteristics of diurnal rainfall over Borneo and surrounding oceans as observed by TRMM-PR. *Journal of Climate*, *19*(7), 1238–1260. <https://doi.org/10.1175/JCLI3714.1>
- Im, E. S., & Eltahir, E. A. B. (2018). Simulation of the diurnal variation of rainfall over the western Maritime Continent using a regional climate model. *Climate Dynamics*, *51*(1–2), 73–88. <https://doi.org/10.1007/s00382-017-3907-3>
- Inoue, K., Adames, Á. F., & Yasunaga, K. (2020). Vertical Velocity Profiles in Convectively Coupled Equatorial Waves and MJO: New Diagnoses of Vertical Velocity Profiles in the Wavenumber–Frequency Domain. *Journal of the Atmospheric Sciences*, *77*(6), 2139–2162. <https://doi.org/10.1175/JAS-D-19-0209.1>
- Janiga, M. A., & Zhang, C. (2016). MJO Moisture Budget during DYNAMO in a Cloud-Resolving Model. *Journal of the Atmospheric Sciences*, *73*(6), 2257–2278. <https://doi.org/10.1175/JAS-D-14-0379.1>
- Johnson, R. H., & Nicholls, M. E. (1983). A Composite Analysis of the Boundary Layer Accompanying a Tropical Squall Line. *Monthly Weather Review*, *111*(2), 308–319. [https://doi.org/10.1175/1520-0493\(1983\)111<0308:ACAOTB>2.0.CO;2](https://doi.org/10.1175/1520-0493(1983)111<0308:ACAOTB>2.0.CO;2)
- Kamimera, H., Mori, S., Yamanaka, M. D., & Syamsudin, F. (2012). Modulation of Diurnal Rainfall Cycle by the Madden-Julian Oscillation Based on One-Year Continuous Observations with a Meteorological Radar in West Sumatera. *SOLA*, *8*, 111–114. <https://doi.org/10.2151/sola.2012-028>
- Keenan, T., Rutledge, S., Carbone, R., Wilson, J., Takahashi, T., May, P., et al. (2000). The Maritime Continent — Thunderstorm Experiment (MCTEX): Overview and Some Results. *Bulletin of the American Meteorological Society*, *81*(10), 2433–2456. [https://doi.org/10.1175/1520-0477\(2000\)081<2433:TMCTEM>2.3.CO;2](https://doi.org/10.1175/1520-0477(2000)081<2433:TMCTEM>2.3.CO;2)

- Keenan, T. D., Morton, B. R., Manton, M. J., & Holland, G. J. (1989). The Island Thunderstorm Experiment (ITEX)—A Study of Tropical Thunderstorms in the Maritime Continent. *Bulletin of the American Meteorological Society*, *70*(2), 152–159. [https://doi.org/10.1175/1520-0477\(1989\)070<0152:TITESO>2.0.CO;2](https://doi.org/10.1175/1520-0477(1989)070<0152:TITESO>2.0.CO;2)
- Kikuchi, K., & Wang, B. (2008). Diurnal Precipitation Regimes in the Global Tropics. *Journal of Climate*, *21*(11), 2680–2696. <https://doi.org/10.1175/2007JCLI2051.1>
- Kim, D., Ahn, M.-S., Kang, I.-S., & Del Genio, A. D. (2015). Role of Longwave Cloud–Radiation Feedback in the Simulation of the Madden–Julian Oscillation. *Journal of Climate*, *28*(17), 6979–6994. <https://doi.org/10.1175/JCLI-D-14-00767.1>
- Kim, H., Lee, M.-I., Cha, D.-H., Lim, Y.-K., & Putman, W. M. (2019). Improved representation of the diurnal variation of warm season precipitation by an atmospheric general circulation model at a 10 km horizontal resolution. *Climate Dynamics*, *53*(11), 6523–6542. <https://doi.org/10.1007/s00382-019-04943-6>
- Krueger, S. K., Fu, Q., Liou, K. N., & Chin, H.-N. S. (1995). Improvements of an Ice-Phase Microphysics Parameterization for Use in Numerical Simulations of Tropical Convection. *Journal of Applied Meteorology*, *34*(1), 281–287. <https://doi.org/10.1175/1520-0450-34.1.281>
- Kummerow, C., Simpson, J., Thiele, O., Barnes, W., Chang, A. T. C., Stocker, E., et al. (2000). The Status of the Tropical Rainfall Measuring Mission (TRMM) after Two Years in Orbit. *Journal of Applied Meteorology*, *39*(12), 1965–1982. [https://doi.org/10.1175/1520-0450\(2001\)040<1965:TSOTTR>2.0.CO;2](https://doi.org/10.1175/1520-0450(2001)040<1965:TSOTTR>2.0.CO;2)
- Lang, S., Tao, W.-K., Simpson, J., Cifelli, R., Rutledge, S., Olson, W., & Halverson, J. (2007). Improving Simulations of Convective Systems from TRMM LBA: Easterly and Westerly Regimes. *Journal of the Atmospheric Sciences*, *64*(4), 1141–1164. <https://doi.org/10.1175/JAS3879.1>
- Liebmann, B., & Smith, C. A. (1996). Description of a complete (interpolated) outgoing longwave radiation dataset. *Bulletin of the American Meteorological Society*, *77*, 1275–1277.
- Liebmann, Brant, & Hartmann, D. L. (1982). Interannual Variations of Outgoing IR Associated with Tropical Circulation Changes During 1974–78. *Journal of the Atmospheric Sciences*, *39*(5), 1153–1162. [https://doi.org/10.1175/1520-0469\(1982\)039<1153:IVOOIA>2.0.CO;2](https://doi.org/10.1175/1520-0469(1982)039<1153:IVOOIA>2.0.CO;2)
- Lin, J.-L., & Mapes, B. E. (2004). Radiation Budget of the Tropical Intraseasonal Oscillation. *Journal of the Atmospheric Sciences*, *61*(16), 2050–2062. [https://doi.org/10.1175/1520-0469\(2004\)061<2050:RBOTTI>2.0.CO;2](https://doi.org/10.1175/1520-0469(2004)061<2050:RBOTTI>2.0.CO;2)
- Love, B. S., Matthews, A. J., & Lister, G. M. S. (2011). The diurnal cycle of precipitation over the Maritime Continent in a high-resolution atmospheric model. *Quarterly Journal of the Royal Meteorological Society*, *137*(657), 934–947. <https://doi.org/10.1002/qj.809>
- Madden, R. A., & Julian, P. R. (1971). Detection of a 40–50 Day Oscillation in the Zonal Wind in the Tropical Pacific. *Journal of the Atmospheric Sciences*, *28*(5), 702–708. [https://doi.org/10.1175/1520-0469\(1971\)028<0702:DOADOI>2.0.CO;2](https://doi.org/10.1175/1520-0469(1971)028<0702:DOADOI>2.0.CO;2)

- Madden, R. A., & Julian, P. R. (1972). Description of Global-Scale Circulation Cells in the Tropics with a 40–50 Day Period. *Journal of the Atmospheric Sciences*, 29(6), 1109–1123. [https://doi.org/10.1175/1520-0469\(1972\)029<1109:DOGSCC>2.0.CO;2](https://doi.org/10.1175/1520-0469(1972)029<1109:DOGSCC>2.0.CO;2)
- Mapes, B. E., Warner, T. T., Xu, M., & Negri, A. J. (2003). Diurnal patterns of rainfall in northwestern South America. Part I: Observations and context. *Monthly Weather Review*, 131(5), 799–812. [https://doi.org/10.1175/1520-0493\(2003\)131<0799:DPORIN>2.0.CO;2](https://doi.org/10.1175/1520-0493(2003)131<0799:DPORIN>2.0.CO;2)
- Mapes, B. E., Warner, T. T., & Xu, M. (2003). Diurnal patterns of rainfall in northwestern South America. Part III: Diurnal gravity waves and nocturnal convection offshore. *Monthly Weather Review*, 131(5), 830–844. [https://doi.org/10.1175/1520-0493\(2003\)131<0830:DPORIN>2.0.CO;2](https://doi.org/10.1175/1520-0493(2003)131<0830:DPORIN>2.0.CO;2)
- Mapes, B. E., Chung, E. S., Hannah, W. M., Masunaga, H., Wimmers, A. J., & Velden, C. S. (2018). The Meandering Margin of the Meteorological Moist Tropics. *Geophysical Research Letters*, 45(2), 1177–1184. <https://doi.org/doi:10.1002/2017GL076440>
- Mizuta, R., Oouchi, K., Yoshimura, H., Noda, A., Katayama, K., Yukimoto, S., et al. (2006). 20-km-Mesh Global Climate Simulations Using JMA-GSM Model —Mean Climate States—. *Journal of the Meteorological Society of Japan. Ser. II*, 84(1), 165–185. <https://doi.org/10.2151/jmsj.84.165>
- Mori, S., Jun-Ichi, H., Tauhid, Y. I., Yamanaka, M. D., Okamoto, N., Murata, F., et al. (2004). Diurnal Land–Sea Rainfall Peak Migration over Sumatera Island, Indonesian Maritime Continent, Observed by TRMM Satellite and Intensive Rawinsonde Soundings. *Monthly Weather Review*, 132(8), 2021–2039. [https://doi.org/10.1175/1520-0493\(2004\)132<2021:DLRPMO>2.0.CO;2](https://doi.org/10.1175/1520-0493(2004)132<2021:DLRPMO>2.0.CO;2)
- Mori, S., Hamada, J.-I., Sakurai, N., Fudeyasu, H., Kawashima, M., Hashiguchi, H., et al. (2011). Convective Systems Developed along the Coastline of Sumatera Island, Indonesia, Observed with an X-band Doppler Radar during the HARIMAU2006 Campaign. *Journal of the Meteorological Society of Japan*, 89A, 61–81. <https://doi.org/10.2151/jmsj.2011-a04>
- Mori, S., Hamada, J.-I., Hattori, M., Wu, P.-M., Katsumata, M., Endo, N., et al. (2018). Meridional march of diurnal rainfall over Jakarta, Indonesia, observed with a C-band Doppler radar: an overview of the HARIMAU2010 campaign. *Progress in Earth and Planetary Science*, 5(1), 47. <https://doi.org/10.1186/s40645-018-0202-9>
- Morrison, H., Thompson, G., & Tatarskii, V. (2009). Impact of Cloud Microphysics on the Development of Trailing Stratiform Precipitation in a Simulated Squall Line: Comparison of One- and Two-Moment Schemes. *Monthly Weather Review*, 137(3), 991–1007. <https://doi.org/10.1175/2008MWR2556.1>
- Muller, C. J., & Held, I. M. (2012). Detailed Investigation of the Self-Aggregation of Convection in Cloud-Resolving Simulations. *Journal of the Atmospheric Sciences*, 69(8), 2551–2565. <https://doi.org/10.1175/JAS-D-11-0257.1>
- Nakanishi, M., & Niino, H. (2009). Development of an Improved Turbulence Closure Model for the Atmospheric Boundary Layer. *Journal of the Meteorological Society of Japan. Ser. II*, 87(5), 895–912. <https://doi.org/10.2151/jmsj.87.895>

- Neale, R., & Slingo, J. (2003). The Maritime Continent and its role in the global climate: A GCM study. *Journal of Climate*, *16*(5), 834–848. [https://doi.org/10.1175/1520-0442\(2003\)016<0834:TMCAIR>2.0.CO;2](https://doi.org/10.1175/1520-0442(2003)016<0834:TMCAIR>2.0.CO;2)
- Neelin, J. D., Peters, O., & Hales, K. (2009). The Transition to Strong Convection. *Journal of the Atmospheric Sciences*, *66*(8), 2367–2384. <https://doi.org/10.1175/2009JAS2962.1>
- Nesbitt, S. W., & Zipser, E. J. (2003). The Diurnal Cycle of Rainfall and Convective Intensity according to Three Years of TRMM Measurements. *Journal of Climate*, *16*(10), 1456–1475. <https://doi.org/10.1175/1520-0442-16.10.1456>
- Ogino, S.-Y., Yamanaka, M. D., Mori, S., & Matsumoto, J. (2016). How Much is the Precipitation Amount over the Tropical Coastal Region? *Journal of Climate*, *29*(3), 1231–1236. <https://doi.org/10.1175/JCLI-D-15-0484.1>
- Ogura, Y., & Yoshizaki, M. (1988). Numerical study of orographic-convective precipitation over the eastern Arabian Sea and the Ghat Mountains during the summer monsoon. *Journal of the Atmospheric Sciences*, *45*(15), 2097–2122. [https://doi.org/10.1175/1520-0469\(1988\)045<2097:NSOOC>2.0.CO;2](https://doi.org/10.1175/1520-0469(1988)045<2097:NSOOC>2.0.CO;2)
- Okamoto, K., Ushio, T., Iguchi, T., Takahashi, N., & Iwanami, K. (2005). The Global Satellite Mapping of Precipitation (GSMaP) project. In *International Geoscience and Remote Sensing Symposium (IGARSS)* (Vol. 5, pp. 3414–3416). IEEE. <https://doi.org/10.1109/IGARSS.2005.1526575>
- Reynolds, R. W., Smith, T. M., Liu, C., Chelton, D. B., Casey, K. S., & Schlax, M. G. (2007). Daily High-Resolution-Blended Analyses for Sea Surface Temperature. *Journal of Climate*, *20*(22), 5473–5496. <https://doi.org/10.1175/2007JCLI1824.1>
- Rushley, S. S., Kim, D., Bretherton, C. S., & Ahn, M.-S. (2018). Reexamining the Nonlinear Moisture-Precipitation Relationship Over the Tropical Oceans. *Geophysical Research Letters*, *45*(2), 1133–1140. <https://doi.org/doi:10.1002/2017GL076296>
- Sakaeda, N., Kiladis, G., & Dias, J. (2020). The Diurnal Cycle of Rainfall and the Convectively Coupled Equatorial Waves over the Maritime Continent. *Journal of Climate*, *33*(8), 3307–3331. <https://doi.org/10.1175/JCLI-D-19-0043.1>
- Sakurai, N., Murata, F., Yamanaka, M. D., Mori, S., Hamada, J. I., Hashiguchi, H., et al. (2005). Diurnal cycle of cloud system migration over Sumatera Island. *Journal of the Meteorological Society of Japan*, *83*(5), 835–850. <https://doi.org/10.2151/jmsj.83.835>
- Sakurai, N., Kawashima, M., Fujiyoshi, Y., Hashiguchi, H., Shimomai, T., Mori, S., et al. (2009). Internal structures of migratory cloud systems with diurnal cycle over Sumatera Island during CPEA-I campaign. *Journal of the Meteorological Society of Japan*, *87*(1), 157–170. <https://doi.org/10.2151/jmsj.87.157>
- Salby, M. L., Hendon, H. H., Woodberry, K., & Tanaka, K. (1991). Analysis of Global Cloud Imagery from Multiple Satellites. *Bulletin of the American Meteorological Society*, *72*(4), 467–480. [https://doi.org/10.1175/1520-0477\(1991\)072<0467:AOGCIF>2.0.CO;2](https://doi.org/10.1175/1520-0477(1991)072<0467:AOGCIF>2.0.CO;2)
- Sato, T., Miura, H., Satoh, M., Takayabu, Y. N., & Wang, Y. (2009). Diurnal Cycle of Precipitation in the Tropics Simulated in a Global Cloud-Resolving Model. *Journal of Climate*, *22*(18), 4809–4826. <https://doi.org/10.1175/2009JCLI2890.1>

- Sato, Y., Nishizawa, S., Yashiro, H., Miyamoto, Y., Kajikawa, Y., & Tomita, H. (2015). Impacts of cloud microphysics on trade wind cumulus: which cloud microphysics processes contribute to the diversity in a large eddy simulation? *Progress in Earth and Planetary Science*, 2(1), 23. <https://doi.org/10.1186/s40645-015-0053-6>
- Saxen, T. R., & Rutledge, S. A. (1998). Surface Fluxes and Boundary Layer Recovery in TOGA COARE: Sensitivity to Convective Organization. *Journal of the Atmospheric Sciences*, 55(17), 2763–2781. [https://doi.org/10.1175/1520-0469\(1998\)055<2763:SFABLR>2.0.CO;2](https://doi.org/10.1175/1520-0469(1998)055<2763:SFABLR>2.0.CO;2)
- Schiro, K. A., Neelin, J. D., Adams, D. K., & Lintner, B. R. (2016). Deep Convection and Column Water Vapor over Tropical Land versus Tropical Ocean: A Comparison between the Amazon and the Tropical Western Pacific. *Journal of the Atmospheric Sciences*, 73(10), 4043–4063. <https://doi.org/10.1175/JAS-D-16-0119.1>
- Sekiguchi, M., & Nakajima, T. (2008). A k-distribution-based radiation code and its computational optimization for an atmospheric general circulation model. *Journal of Quantitative Spectroscopy and Radiative Transfer*, 109(17), 2779–2793. <https://doi.org/https://doi.org/10.1016/j.jqsrt.2008.07.013>
- Shige, S., Nakano, Y., & Yamamoto, M. K. (2017). Role of orography, diurnal cycle, and intraseasonal oscillation in summer monsoon rainfall over the western ghats and myanmar coast. *Journal of Climate*, 30(23), 9365–9381. <https://doi.org/10.1175/JCLI-D-16-0858.1>
- Sobel, A., Wang, S., & Kim, D. (2014). Moist Static Energy Budget of the MJO during DYNAMO. *Journal of the Atmospheric Sciences*, 71(11), 4276–4291. <https://doi.org/10.1175/JAS-D-14-0052.1>
- Stan, C., Straus, D. M., Frederiksen, J. S., Lin, H., Maloney, E. D., & Schumacher, C. (2017). Review of Tropical-Extratropical Teleconnections on Intraseasonal Time Scales. *Reviews of Geophysics*, 55(4), 902–937. <https://doi.org/10.1002/2016RG000538>
- Sueki, K., Yamaura, T., Yashiro, H., Nishizawa, S., Yoshida, R., Kajikawa, Y., & Tomita, H. (2019). Convergence of Convective Updraft Ensembles With Respect to the Grid Spacing of Atmospheric Models. *Geophysical Research Letters*, 46(24), 14817–14825. <https://doi.org/10.1029/2019GL084491>
- Tanji, S., & Inatsu, M. (2019). Case Study of Blowing Snow Potential Diagnosis with Dynamical Downscaling. *SOLA*, 15, 32–36. <https://doi.org/10.2151/sola.2019-007>
- Thornberry, T. D., Rollins, A. W., Avery, M. A., Woods, S., Lawson, R. P., Bui, T. V., & Gao, R.-S. (2017). Ice water content-extinction relationships and effective diameter for TTL cirrus derived from in situ measurements during ATTREX 2014. *Journal of Geophysical Research: Atmospheres*, 122(8), 4494–4507. <https://doi.org/10.1002/2016JD025948>
- Tomita, H. (2008). New Microphysical Schemes with Five and Six Categories by Diagnostic Generation of Cloud Ice. *Journal of the Meteorological Society of Japan. Ser. II*, 86A, 121–142. <https://doi.org/10.2151/jmsj.86A.121>
- Ulate, M., Dudhia, J., & Zhang, C. (2014). Sensitivity of the water cycle over the Indian Ocean and Maritime Continent to parameterized physics in a regional model. *Journal of Advances in Modeling Earth Systems*, 6(4), 1095–1120. <https://doi.org/10.1002/2014MS000313>

- Vincent, C. L., & Lane, T. P. (2016). Evolution of the Diurnal Precipitation Cycle with the Passage of a Madden–Julian Oscillation Event through the Maritime Continent. *Monthly Weather Review*, *144*(5), 1983–2005. <https://doi.org/10.1175/mwr-d-15-0326.1>
- Vincent, C. L., & Lane, T. P. (2017). A 10-Year Austral Summer Climatology of Observed and Modeled Intraseasonal, Mesoscale, and Diurnal Variations over the Maritime Continent. *Journal of Climate*, *30*(10), 3807–3828. <https://doi.org/10.1175/JCLI-D-16-0688.1>
- Wainwright, C. E., Dawson, D. T., Xue, M., & Zhang, G. (2014). Diagnosing the Intercept Parameters of the Exponential Drop Size Distributions in a Single-Moment Microphysics Scheme and Impact on Supercell Storm Simulations. *Journal of Applied Meteorology and Climatology*, *53*(8), 2072–2090. <https://doi.org/10.1175/JAMC-D-13-0251.1>
- Wing, A. A., & Emanuel, K. (2014). Physical mechanisms controlling self-aggregation of convection in idealized numerical modeling simulations. *Journal of Advances in Modeling Earth Systems*, n/a-n/a. <https://doi.org/10.1002/2013MS000269>
- Wolding, B. O., & Maloney, E. D. (2015). Objective Diagnostics and the Madden–Julian Oscillation. Part II: Application to Moist Static Energy and Moisture Budgets. *Journal of Climate*, *28*(19), 7786–7808. <https://doi.org/10.1175/JCLI-D-14-00689.1>
- Wu, P., Manabu, D. Y., & Matsumoto, J. (2008). The Formation of Nocturnal Rainfall Offshore from Convection over Western Kalimantan (Borneo) Island. *Journal of the Meteorological Society of Japan. Ser. II*, *86A*, 187–203. <https://doi.org/10.2151/jmsj.86A.187>
- Wu, P., Hara, M., Hamada, J., Yamanaka, M. D., & Kimura, F. (2009). Why a Large Amount of Rain Falls over the Sea in the Vicinity of Western Sumatra Island during Nighttime. *Journal of Applied Meteorology and Climatology*, *48*(7), 1345–1361. <https://doi.org/10.1175/2009JAMC2052.1>
- Xie, S. P., Xu, H., Saji, N. H., Wang, Y., & Liu, W. T. (2006). Role of narrow mountains in large-scale organization of Asian Monsoon convection. *Journal of Climate*, *19*(14), 3420–3429. <https://doi.org/10.1175/JCLI3777.1>
- Yamanaka, M. D. (2016). Physical climatology of Indonesian maritime continent: An outline to comprehend observational studies. *Atmospheric Research*, *178–179*, 231–259. <https://doi.org/https://doi.org/10.1016/j.atmosres.2016.03.017>
- Yanase, A., Yasunaga, K., & Masunaga, H. (2017). Relationship between the direction of diurnal rainfall migration and the ambient wind over the Southern Sumatra Island. *Earth and Space Science*, *4*(3). <https://doi.org/10.1002/2016EA000181>
- Yang, G.-Y., & Slingo, J. (2001). The Diurnal Cycle in the Tropics. *Monthly Weather Review*, *129*(4), 784–801. [https://doi.org/10.1175/1520-0493\(2001\)129<0784:TDCITT>2.0.CO;2](https://doi.org/10.1175/1520-0493(2001)129<0784:TDCITT>2.0.CO;2)
- Yang, S., & Smith, E. A. (2006). Mechanisms for Diurnal Variability of Global Tropical Rainfall Observed from TRMM. *Journal of Climate*, *19*(20), 5190–5226. <https://doi.org/10.1175/JCLI3883.1>
- Yang, S., Zhang, T., Li, Z., & Dong, S. (2019). Climate Variability over the Maritime Continent and Its Role in Global Climate Variation: A Review. *Journal of Meteorological Research*, *33*(6), 993–1015. <https://doi.org/10.1007/s13351-019-9025-x>

- Yasunaga, K., & Mapes, B. (2012). Differences between More Divergent and More Rotational Types of Convectively Coupled Equatorial Waves. Part I: Space–Time Spectral Analyses. *Journal of the Atmospheric Sciences*, *69*(1), 3–16. <https://doi.org/10.1175/JAS-D-11-033.1>
- Yasunaga, K., Yokoi, S., Inoue, K., & Mapes, B. E. (2018). Space–Time Spectral Analysis of the Moist Static Energy Budget Equation. *Journal of Climate*, *32*(2), 501–529. <https://doi.org/10.1175/JCLI-D-18-0334.1>
- Yihui, D., Chongyin, L., & Yanju, L. (2004). Overview of the South China sea monsoon experiment. *Advances in Atmospheric Sciences*, *21*(3), 343–360. <https://doi.org/10.1007/BF02915563>
- Yokoi, S. (2020). Diurnal variation of surface heat fluxes off the west coast of Sumatra Island as revealed by in situ observation. *SOLA, advpub*. <https://doi.org/10.2151/sola.16A-001>
- Yokoi, S., Katsumata, M., & Yoneyama, K. (2014). Variability in surface meteorology and air–sea fluxes due to cumulus convective systems observed during CINDY/DYNAMO. *Journal of Geophysical Research: Atmospheres*, *119*(5), 2064–2078. <https://doi.org/10.1002/2013JD020621>
- Yokoi, S., Mori, S., Katsumata, M., Geng, B., Yasunaga, K., Syamsudin, F., et al. (2017a). Diurnal cycle of precipitation observed in the western coastal area of Sumatra Island: Offshore preconditioning by gravity waves. *Monthly Weather Review*, *145*(9). <https://doi.org/10.1175/MWR-D-16-0468.1>
- Yokoi, S., Mori, S., Katsumata, M., Geng, B., Yasunaga, K., Syamsudin, F., et al. (2017b). Diurnal Cycle of Precipitation Observed in the Western Coastal Area of Sumatra Island: Offshore Preconditioning by Gravity Waves. *Monthly Weather Review*, *145*(9), 3745–3761. <https://doi.org/10.1175/mwr-d-16-0468.1>
- Yoshida, R., Nishizawa, S., Yashiro, H., Adachi, S. A., Yamaura, T., Tomita, H., & Kajikawa, Y. (2019). Maintenance condition of back-building squall-line in a numerical simulation of a heavy rainfall event in July 2010 in Western Japan. *Atmospheric Science Letters*, *20*(1), e880. <https://doi.org/10.1002/asl.880>
- Young, G. S., Perugini, S. M., & Fairall, C. W. (1995). Convective Wakes in the Equatorial Western Pacific during TOGA. *Monthly Weather Review*, *123*(1), 110–123. [https://doi.org/10.1175/1520-0493\(1995\)123<0110:CWITEW>2.0.CO;2](https://doi.org/10.1175/1520-0493(1995)123<0110:CWITEW>2.0.CO;2)
- Zuidema, P. (2003). Convective clouds over the bay of Bengal. *Monthly Weather Review*, *131*(5), 780–798. [https://doi.org/10.1175/1520-0493\(2003\)131<0780:CCOTBO>2.0.CO;2](https://doi.org/10.1175/1520-0493(2003)131<0780:CCOTBO>2.0.CO;2)
- Zuidema, P., Li, Z., Hill, R. J., Bariteau, L., Rilling, B., Fairall, C., et al. (2011). On Trade Wind Cumulus Cold Pools. *Journal of the Atmospheric Sciences*, *69*(1), 258–280. <https://doi.org/10.1175/JAS-D-11-0143.1>